



NATIONAL TECHNICAL UNIVERSITY OF ATHENS
SCHOOL OF ELECTRICAL AND COMPUTER ENGINEERING
SCHOOL OF MECHANICAL ENGINEERING

INTERDISCIPLINARY POSTGRADUATE PROGRAMME
“Translational Engineering in Health and Medicine”

***MAXIMAL COUPLING BETWEEN IMPLANTED DIPOLE ANTENNAS
AND EXTERNAL SOURCES***

Postgraduate Diploma Thesis

VARVARA P. MOUZI

Supervisor: Dr. Konstantina, S. Nikita

Professor in School of Electrical Engineer, National Technical University of Athens

Co-Supervisor: Dr. Constantinos, Valagiannopoulos

Assistant Professor in School of Electrical Engineer, National Technical University of Athens

Athens, (*June 2024*)



NATIONAL TECHNICAL UNIVERSITY OF ATHENS
SCHOOL OF ELECTRICAL AND COMPUTER ENGINEERING
SCHOOL OF MECHANICAL ENGINEERING

INTERDISCIPLINARY POSTGRADUATE PROGRAMME
“Translational Engineering in Health and Medicine”

**MAXIMAL COUPLING BETWEEN IMPLANTED DIPOLE
ANTENNAS AND EXTERNAL SOURCES**

Postgraduate Diploma Thesis

VARVARA P. MOUZI

Supervisor: Dr. Konstantina, S. Nikita

Professor in School of Electrical Engineer, National Technical University of Athens

Co-Supervisor: Dr. Constantinos, Valagiannopoulos

Assistant Professor in School of Electrical Engineer, National Technical University of Athens

The postgraduate diploma thesis has been approved by the examination committee
on (*exam day: 9th July 2024*)

1st member

2nd member

3rd member

*Dr. Konstantina, S. Nikita
Professor in School of
Electrical Engineer, National
Technical University of
Athens*

*Dr. Constantinos,
Valagiannopoulos
Assistant Professor in School
of Electrical Engineer,
National Technical
University of Athens*

*Dr. Spyretta Golemati
Associate Professor in
School of Medicine, National
and Kapodistrian University
of Athens*

Athens, (June 2024)

.....

Varvara P. Mouzi
Graduate of the Interdisciplinary Postgraduate Programme,
“Translational Engineering in Health and Medicine”,
Master of Science,
School of Electrical and Computer Engineering,
National Technical University of Athens

Copyright © - *Varvara P. Mouzi, 2024*

All rights reserved.

You may not copy, reproduce, distribute, publish, display, modify, create derivative works, transmit, or in any way exploit this thesis or part of it for commercial purposes. You may reproduce, store or distribute this thesis for non-profit educational or research purposes, provided that the source is cited, and the present copyright notice is retained. Inquiries for commercial use should be addressed to the original author.

The ideas and conclusions presented in this paper are the author's and do not necessarily reflect the official views of the National Technical University of Athens.

Summary

In recent years, the field of biomedical engineering has witnessed significant advancements in implantable devices designed for healthcare monitoring, diagnostic imaging, and therapeutic interventions. Wireless power transfer to these implantable devices is crucial for their efficient operation. However, optimizing the coupling between external electromagnetic (EM) sources and implanted dipole antennas within the human body presents several challenges, primarily due to the complex dielectric properties of biological tissues. This thesis addresses these challenges by proposing innovative methods to enhance signal transmission and improve the efficiency of wireless power transfer to implanted biosensors, thereby advancing the capabilities of medical telemetry systems.

The methods section focuses on the excitation and operation frequency for optimal coupling between external sources and implanted antennas. Two primary approaches are explored: dielectric layers forming Fabry-Perot resonant cavities and active EM metasurfaces incorporating gain media.

The first method utilizes dielectric layers to enhance the coupling efficiency by optimizing resonance conditions. The dielectric materials are chosen based on their properties to form resonant cavities, which maximize EM wave transmission between the implanted antenna and the external source, improving signal strength and clarity. The setup aims to minimize reflections and enhance the coupling between the antennas by creating an optimal resonant environment.

The second approach involves the use of active metasurfaces incorporating gain media. These metasurfaces provide a high degree of control over EM wave propagation, allowing for precise engineering to manipulate EM waves and achieve optimal matching conditions. The active nature of the metasurfaces boosts transmissivity, significantly enhancing the coupling efficiency. This approach offers robust performance even in the presence of misalignment between the implanted and external antennas.

Mathematical models are developed to predict the optimal configurations for both methods, taking into account the complex dielectric properties of biological tissues. These models provide a theoretical framework for understanding the interaction between EM waves and biological tissues, facilitating the design of optimized coupling mechanisms.

Extensive computational simulations are conducted to validate the theoretical predictions. These simulations consider various scenarios, including different distances and misalignment between the implanted and external antennas. The simulations focus on the robustness of the matching components, demonstrating their practical applicability in real-world biomedical settings.

The results of the study highlight the effectiveness of both proposed methods in enhancing coupling efficiency between implanted dipole antennas and external sources. Key findings from the simulations and mathematical modeling include:

Optimal Matching Layer: The dielectric layers forming Fabry-Perot resonant cavities significantly improve coupling efficiency. The simulations show that this setup can achieve high coupling efficiency by optimizing resonance conditions, resulting in improved signal transmission and clarity. The optimal configurations for the dielectric layers are identified, demonstrating their effectiveness in various scenarios, including different distances and misalignments.

Optimal Matching Metasurface: The active EM metasurfaces with gain media provide a higher degree of control over EM wave propagation, resulting in superior coupling efficiency. The simulations reveal that these metasurfaces can achieve optimal matching conditions, significantly boosting coupling efficiency even in the presence of misalignment. The robustness of the active metasurfaces is highlighted, showing that they can maintain high performance under experimental imperfections.

In conclusion, an extensive analysis of the secondary antenna's mismatch across both angles (θ, φ) for a separation distance on transition zone is presented. The results indicate that employing a metasurface as a matching technique results in the highest performance at $\theta = \varphi = 0$, aligning with initial conditions depicted in other figures. Despite achieving higher transmission, there is a more pronounced decrease in performance with increasing misalignment angles compared to the matching layer technique. However, the desired transmission factor values are attained within specific regions, demonstrating that optimal alignment yields the highest transmission efficiency but the system maintains satisfactory performance over a broader range of angles.

The findings of this thesis have significant implications for the design and optimization of medical instruments used in healthcare monitoring, bioelectromagnetic imaging, and diagnostics. By improving the coupling efficiency between implanted and external antennas, these technologies can enhance the reliability and accuracy of medical telemetry systems. This improvement can lead to better patient outcomes through more accurate monitoring of physiological signals. The research also provides insights into the potential applications of advanced EM metasurfaces in biomedical engineering. The ability to precisely control EM wave propagation using metasurfaces opens up new possibilities for designing miniaturized and efficient implantable devices for continuous health monitoring, targeted drug delivery, and other medical applications.

This thesis presents a comprehensive study on optimizing coupling between implanted dipole antennas and external sources. By employing dielectric layers and active EM metasurfaces, the research proposes two effective methods to enhance coupling efficiency. The mathematical models and numerical simulations provide a robust framework for designing optimized biomedical systems. The findings have significant implications for the future development of implantable medical devices, promising improvements in healthcare monitoring, diagnostics, and patient care. This research contributes to the advancement of biomedical engineering by addressing the critical challenge of efficient signal transmission in implantable systems and paving the way for more reliable and effective medical technologies.

Abstract

This thesis investigates the optimization of wireless power transfer between external electromagnetic (EM) sources and implanted dipole antennas within the human body, a critical factor for the effective operation of biosensors in various biomedical applications. The research addresses the complex interaction between implanted antennas and surrounding biological tissues, focusing on enhancing signal transmission. Two innovative approaches are explored to improve the matching between free-space radiators and embedded receivers: the use of dielectric layers forming Fabry-Perot resonant cavities and the deployment of active EM metasurfaces incorporating gain media.

The first approach employs dielectric layers to form Fabry-Perot resonant cavities, which optimize resonance conditions to enhance coupling efficiency. This method is designed to maximize EM wave transmission between the implanted antenna and the external source, thereby improving signal strength and clarity. The second approach involves the use of active metasurfaces with gain media, offering a high degree of control over EM wave propagation. These metasurfaces can be precisely engineered to manipulate EM waves, achieving optimal matching conditions and significantly boosting coupling efficiency.

Mathematical models are developed to predict the optimal configurations for both methods, taking into account the complex dielectric properties of biological tissues. Extensive numerical simulations validate these theoretical predictions, considering various scenarios, including different distances and misalignment between the implanted and external antennas. The robustness of the matching components in these scenarios is emphasized, highlighting their practical applicability in real-world biomedical settings.

The results of this study have significant implications for the design and optimization of medical instruments used in healthcare monitoring, bioelectromagnetic imaging, and diagnostics. By improving the coupling efficiency between implanted and external antennas, these technologies can enhance the reliability and accuracy of medical telemetry systems. This, in turn, can lead to better patient care and outcomes by ensuring more accurate monitoring of physiological signals. Furthermore, the research provides insights into the potential applications of advanced EM metasurfaces in biomedical engineering. The ability to precisely control EM wave propagation using metasurfaces opens up new possibilities for designing miniaturized and efficient implantable devices, which can be used in a wide range of medical applications, from continuous health monitoring to targeted drug delivery systems.

In conclusion, this thesis presents a comprehensive study on optimizing coupling between implanted dipole antennas and external sources. By employing dielectric layers and active EM metasurfaces, the research proposes two effective methods to enhance coupling efficiency. The mathematical models and numerical simulations provide a robust framework for designing optimized biomedical systems. The findings have significant implications for the future development of implantable medical

devices, promising improvements in healthcare monitoring, diagnostics, and patient care. This research contributes to the advancement of biomedical engineering by addressing the critical challenge of efficient signal transmission in implantable systems and paving the way for more reliable and effective medical technologies.

Key terms : Biomedical communication, Electromagnetic coupling, Implants, Metasurfaces, Wireless power transmission, Implantable antennas, Matching Technique

Table of Contents

Summary.....	4
Abstract	6
Table of Contents	8
I.) Introduction	9
a) Background	9
b) Types of Implantable Antennas.....	11
c) Near Field and Far Field.....	14
II.) Methods	16
a) Excitation and Operation Frequency	16
b) Medium Selection.....	17
III.) Results	18
a) Computational Modeling.....	18
b) Mathematical Modeling	21
c) Optimal Matching Layer	23
d) Optimal Matching Metasurface.....	27
IV.) Conclusions and Future Considerations	30
Bibliography.....	32

I.) Introduction

a) Background

Implantable antennas have recently become increasingly popular as they form an indispensable part of modern biometric telemetry systems, enabling the transmission of physiological signals both within and outside the human body [1]. These technologies are crucial for the early detection of diseases, particularly chronic conditions [2], and offer long-term monitoring of patient activities under normal physiological conditions [3], significantly enhancing the quality of life for patients [4]. Consequently, extensive research efforts have been directed at addressing the challenging aspects of implantable devices, such as biocompatibility, miniaturization, patient safety, connectivity with external monitoring or control equipment, and insensitivity to detuning [5].

Several innovative solutions regarding numerical simulations, designs, and employed media have been proposed to overcome the inherent weaknesses of implantable systems, including low data rate, restricted communication range, performance sensitivity to the positioning of various structural parts, and the limitations of invasive endoscopy [6]. For instance, dual-band implantable antennas are utilized for continuous glucose monitoring [7], while folded slot dipoles function safely across the medical band [8]. Additionally, radiators implanted in the skin provide wireless measurements for pressure and temperature [9]. Miniature antennas for integration into head-implanted medical devices have been successfully introduced [10], and parasitic patches placed over the human body have been proposed to enhance the wireless power link between embedded rectennas and external devices [11]. On-body repeaters support wideband transmission [12], and capacitively loaded circularly polarized implanted patches contribute positively to the link budget [13], thereby providing reliable subcutaneous real-time blood measurements [14].

Moreover, recent advancements in implantable devices for biomedical applications show promise in areas such as cancer treatment via hyperthermia, drug delivery, and overall healthcare monitoring. These devices can sense bio-signals like temperature and blood pressure from within the body and transmit this data to external devices, facilitating early diagnosis and prevention of critical medical conditions like heart attacks and strokes [34]. The integration of implantable wireless sensors and microwave imaging systems represents a significant leap forward in medical technology, promising to improve diagnostic accuracy, enhance patient care, and reduce healthcare costs through innovative and efficient solutions [35], [36], [37], [38], [39]. Microwave imaging systems, leveraging the dielectric properties of tissues, are particularly effective for detecting early-stage cancer, hemorrhages, and internal injuries [40], [41], [42], [43]. Their non-ionizing, low-cost, and time-efficient nature makes them a favorable alternative to traditional diagnostic tools like MRI and CT scans, particularly enhancing accessibility and affordability in rural areas [44], [45], [46], [47]. These

technological advances are paving the way for more accessible and efficient diagnostic tools in various medical fields.

In conjunction with these advancements, matching between an electromagnetic (EM) radiator acting as a transmitter and another as a receiver is one of the oldest topics in the scientific domain of wireless links. Effective matching increases the signal-to-noise ratio at the receiver without the need for higher transmission power, regardless of the operating frequency [15]. Examples of this include the deposition of graphene nanoribbons to enhance coupling between optical antennas for improved photocarrier collection [16], the use of matching circuits in multiple-input, multiple-output radio frequency arrays [17], and the installation of passive superstrates to increase the microwave detectability of buried objects [18]. In biomedical applications, wireless power transfer achieved via resonating coils [19] or rectifier circuits [20] is another form of maximal coupling, extensively used in magnetic resonance imaging [21] and implantable sensing [22]. These foundational principles and technologies provide a robust basis for the development of advanced implantable systems.

The advent of electromagnetic metasurfaces has revolutionized the control of EM waves, transforming the traditional laws of reflection and refraction and allowing for the creation of arbitrarily exotic boundary conditions [15]. Impedance matching has now become a special case of the broader concept of controlling waveguide mode propagation and coupling [16]. Metamaterial covers can flexibly tailor the receiving patterns of antennas, greatly benefiting the design and optimization of near-field sensors [17]. Bilayer plasmonic metasurfaces efficiently manipulate visible light [18], block interferences [19], and may employ phase-change active materials to provide tunable optical transmission [20]. Nonlinear elements within these metasurfaces enable efficient frequency mixing with relaxed phase-matching conditions, ideal for broadband frequency conversions and phase conjugation [21]. Strong interference in ultra-thin films has been proposed as an effective mechanism for optical absorption [22], while closed metasurfaces can leverage electromagnetic radiation from multiple sources to achieve green and secure communications [23]. These metasurfaces can also be engineered to control EM fields around and within the human body [24], creating novel optical biosensors that overcome current limitations of bioelectronic interfaces [25].

Building on the principles of effective matching and the advancements in implantable devices, this work combines the two aforementioned topics (implantable antennas, dipole coupling) to treat a simple and frequently met problem comprising one active radiator into free space and another passive receiver embedded into human tissue. Since specific levels of penetrating power are a prerequisite for any biosensor to operate efficiently, re-transmit securely the signals, and record reliably the responses, maximal coupling between the two antennas is vital. Two ways of matching free space with the fat background are proposed: one by depositing dielectric layers and another by utilizing EM metasurfaces. Approximate mathematical models are employed, and the optimal setups are determined with the use of Fabry-Perot resonant cavities in the former scenario and by assuming active structures with gain media in the latter one. Extensive numerical simulations on every radiative region, with commercial software packages, are executed where theoretical predictions are validated while particular

emphasis is given to the case of misaligned dipoles where the robustness of the matching components is demonstrated. The reported results may assist substantially the modeling and design of medical instruments with a wide range of applications from healthcare monitoring and screening to bioelectromagnetic imaging and diagnostics. This research ultimately aims to bridge the gap between theoretical advancements and practical applications in biomedical engineering.

b) Types of Implantable Antennas

In the rapidly advancing field of biomedical engineering, implantable antennas play a crucial role in enhancing the capabilities of various medical devices used for monitoring, diagnostics, and therapeutic interventions. These antennas are designed to operate within the human body, facilitating wireless communication between internal biosensors and external devices. The integration of implantable antennas with medical devices enables continuous health monitoring, real-time data transmission, and effective management of medical conditions. Given the complex environment within the human body, the design and optimization of these antennas require careful consideration of various factors such as biocompatibility, miniaturization, and efficient signal transmission. This section explores the different types of implantable antennas, examining their unique characteristics, frequency operation and design challenges.

Planar Antennas

A probe-fed wideband implantable antenna utilizing a high-permittivity substrate is proposed in [26]. This antenna operates across five frequency bands: 403-405 MHz, 433.1-434.8 MHz, 868-868.6 MHz, 902.8-928.0 MHz, and 2.4-2.48 GHz, exhibiting a notable radiation efficiency of 80% and a wide bandwidth of 168.85%. The gain and specific absorption rate (SAR) are not reported. Another design involves a flexible antenna using Poly-dimethyl Siloxane (PMDS) with lower permittivity as the base material, as proposed by Fu et al. [27]. This antenna operates at 2.42 GHz, with a realized gain of -20.8 dBi and a bandwidth of 10.4%. The SAR is reported to be 156 W/Kg for a 1g average, although the efficiency is not documented. This design is more complex due to the use of shunt capacitances to minimize impedance mismatch.

Wire Antennas

A circularly polarized (CP) helical antenna designed for ingestible capsule applications is proposed in [28], operating at 2.4 GHz with a gain of -19.83 dBi and a bandwidth of 290 MHz. The radiation efficiency is low at -24.8 dB, and SAR is not reported, indicating a lack of patient safety considerations. Another helical antenna design by Xin et al. [29] achieves dual resonance using two non-equally spaced helical copper foil layers. This antenna, tested in a phantom model, operates at 30 MHz with a gain of -67 dBi and an impedance bandwidth of 15.66 MHz (48.21%). The gain is notably low, and neither efficiency nor SAR is reported. A conical spiral antenna operating at 450 MHz with a bandwidth of 101 MHz is presented in [30]. Its performance metrics, including gain, efficiency, and SAR, are not provided, making its overall effectiveness difficult to evaluate.

Conformal Antennas

A conformal CP implantable antenna operating at 2.45 GHz, using Rogers RO6010 as the substrate, is discussed in [31]. It offers a gain of -29.1 dBi and a bandwidth of 31%, but the efficiency is not reported. The SAR is significantly high at 368.7 W/Kg for a 1g average. Despite its large size, the gain could be improved. Another wideband flexible antenna is presented by Das et al. [32], designed on a Kapton polyimide substrate with a Rogers 6010 superstrate. This antenna operates at 2.45 GHz, achieving a bandwidth of 57%, a gain of -9 dBi, and an efficiency of 2.3%, with a SAR of 131 W/Kg. Additionally, a CP implantable slot antenna operating at 915 MHz is discussed in [33], offering a gain of -27 dBi and a bandwidth of 5.7%, with a high SAR value of 517 W/Kg.

Planar Inverted F Antennas (PIFA)

A compact broadband implantable PIFA, operating at 402 MHz, is proposed in [34]. This antenna achieves a gain of -34.9 dBi and a bandwidth of 13%, with a SAR of 284.5 W/Kg at the resonant frequency. Luo et al. [35] have designed a PIFA with a slotted ground plane, operating at 402 MHz and 2.45 GHz. This antenna shows gains of -41 dBi and -21.3 dBi at the respective frequencies, with corresponding bandwidths of 41% and 27.8%. The SAR values are high, at 666 W/Kg and 676 W/Kg, respectively.

Spiral Antennas

Xu et al. propose a CP ring antenna operating at 2.45 GHz, which shows a gain of -22.7 dBi and a bandwidth of 12.4%. The antenna was tested using muscle tissues and has a 1g avg. SAR value of 508 W/Kg at 2.45 GHz. However, the efficiency of the antenna is not reported. The gain should ideally be higher for an antenna of this size [36].

Shah et al. discuss a triband spiral-shaped implantable antenna operating at 402 MHz, 1.6 GHz, and 2.45 GHz, with gains of -30.5 dBi, -22.6 dBi, and -18.2 dBi, respectively. The antenna's bandwidths at these frequencies are 36.8%, 10.8%, and 3.4%. The SAR values at resonant frequencies are relatively high, and the efficiency is not reported [37].

A dual-band CP antenna operating at 902 MHz and 2.45 GHz is proposed by Smanta et al. This antenna exhibits gains of -29.33 dBi and -21.0 dBi, with bandwidths of 12.2% and 123%, respectively. The efficiency is reported to be 2.6% at 920 MHz and 3.8% at 2.45 GHz, but the antenna is noted for its large size [38].

Das et al. present a wideband flexible antenna operating at 2.45 GHz with a gain of -9 dBi and a bandwidth of 57%. The antenna's efficiency is 2.3%, and it has a 1g avg. SAR value of 131 W/Kg at 2.45 GHz. Although it offers a wider bandwidth, it operates at a higher frequency and is relatively large [32].

Slot Antennas

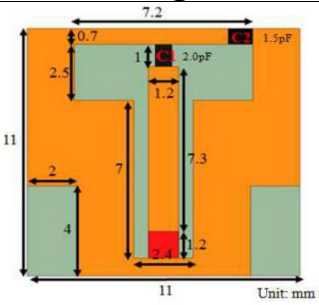
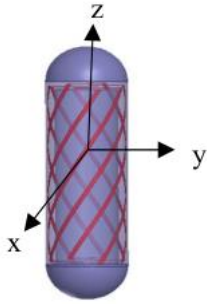

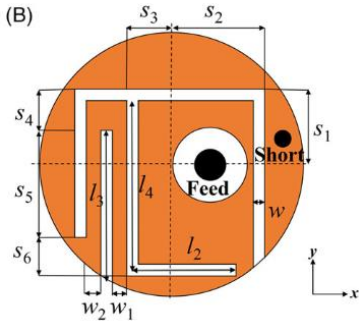
A CP implantable slot antenna operating at 915 MHz is discussed in [33]. This antenna shows a gain of -27 dBi and a bandwidth of 5.7%. The 1g avg. SAR value is 517 W/Kg. This antenna is also noted for its large size.


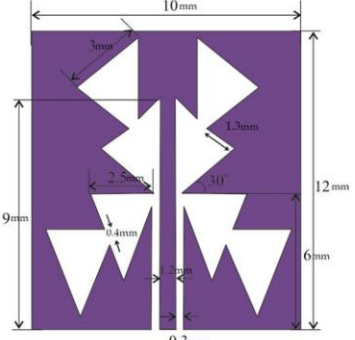
A coplanar waveguide-fed triangular slot antenna operating at 2.45 GHz is proposed in [39]. This antenna demonstrates a peak gain of -7.9 dBi and a bandwidth of 8.2%, with

a radiation efficiency of 0.5% and a 1g avg. SAR value of 136 W/Kg. Despite its very good gain, the antenna's size is relatively large.

Dipole Antenna

A folded dipole antenna designed for UHF (0.951-0.956 GHz) is proposed in [40]. This antenna achieves a maximum gain of -23.5 dBi when used on a human arm. The antenna's electrical size at this frequency contributes to the larger gain despite higher attenuation. Better matching was observed without a glass coating, suggesting the need for robust evaluations in different tissue models to assess matching with glass coating.

Type of Antenna	Reference/Title	Design
Planar	[27]: 'Flexible antenna design on PDMS substrate for implantable bioelectronics applications'	
Wire	[28]: 'Octafilar Helical Antenna for Circular Polarization Wireless Capsule Endoscopy Applications'	
Conformal	[31]: 'A Conformal Circularly Polarized Antenna for Wireless Capsule Endoscope Systems'	
PIFA	[35]: 'Compact dual-band antenna with slotted ground for implantable applications'	

Spiral	[37]: ‘Design and Analysis of a Compact-Sized Multiband Spiral-Shaped Implantable Antenna for Scalp Implantable and Leadless Pacemaker Systems’	
Slot	[39]: ‘Coplanar waveguide-fed ISM band implantable crossed-type triangular slot antenna for biomedical applications’	

A comparison of various implantable antennas reveals diverse performance characteristics, employing different miniaturization techniques. Techniques such as using high-permittivity substrates [41], capacitive loading [27], and radiator current path lengthening [37] are employed for miniaturization. Generally, larger antennas tend to have higher gains, but miniaturization techniques and antenna design specifics, such as slotted versus solid ground planes, significantly impact performance. The implantation depth and the tissue type also contribute to variations in antenna gain due to differing permittivity and conductivity at various frequencies.

c) Near Field and Far Field

An antenna’s radiated electromagnetic field can be divided into two broad regions: the near-field and far-field. The near-field can be further divided into two regions, the non-radiative (reactive) region and the radiative (Fresnel) region.

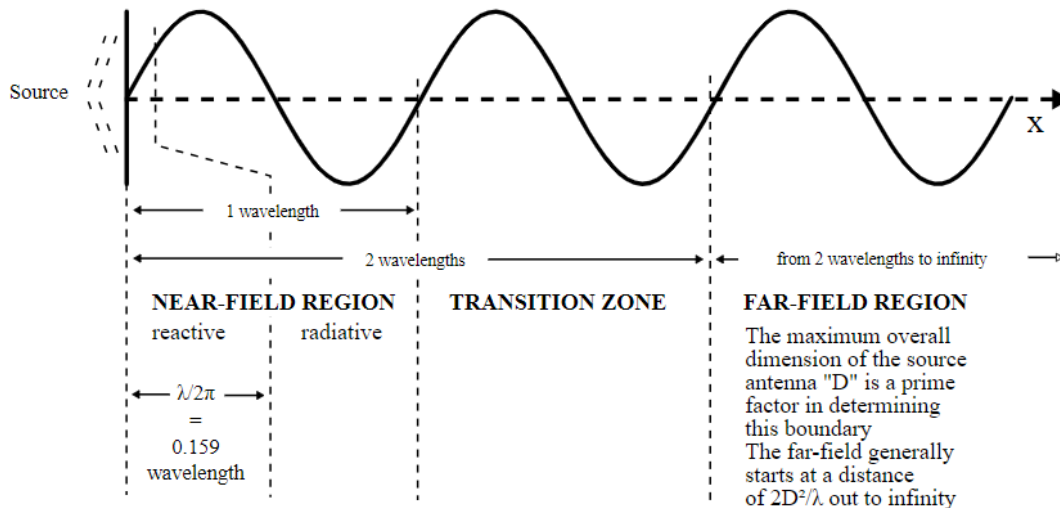


Figure 1.) Field regions for antennas equal to, or shorter than, one-half wavelength of the radiation they emit [42]

Antennas designed to operate in free space or air exhibit different characteristics when placed in the near field of or on the human body. This change in characteristics arises because the operational environment shifts to a material with different dielectric properties. Therefore, it is crucial to analyze both the far-field and near-field radiation characteristics of an antenna for certain applications. In [43], the near-field radiation pattern and the near-field and far-field fidelity factors are explored to determine the performance of the antenna. For biomedical applications, the antennas in [43], [44], [45], [46], [47], [48], [49], [50] are characterized for both near-field and far-field to understand the operational principles of the antenna radiation.

Another significant aspect influenced by the selected operating frequency is the spatial distribution of the field regions, as they substantially modify the behavior of the radiated power. As it is shown in Fig.1, the boundary between the near-field and the far-field regions in electrically small antennas ranges from 1 to 2 times the wavelength, and the reactive near-field zone extends up to a distance of $\lambda/2\pi$. The reactive region greatly impacts the behavior of the radiated power of the antenna, as reported in [4], [51]. When implanted in biological tissue, the surrounding lossy medium dramatically decreases the radiation efficiency of the antenna due to its interaction with the reactive near-field.

II.) Methods

a) Excitation and Operation Frequency

In designing antennas for biomedical applications, selecting an appropriate frequency within the microwave regime is crucial. Various frequency ranges have been identified in the literature as optimal for biomedical diagnostics. Higher frequencies, while providing better resolution, face challenges in penetrating through the human head due to shorter wavelengths and increased interaction with inhomogeneities. Conversely, at lower frequencies, biological tissues exhibit high loss, making these frequencies less practical for such applications [52], [53]. The overall structure of the antenna for low frequencies also becomes large, which can render it impractical for operation near the human body. The frequency band from 1 GHz to 2 GHz has been stated as suitable for medical diagnosis, achieving increased penetration with low power radiation to reduce SAR [43].

Historically, inductive couplings at frequencies below 15 MHz were the first methods of wireless communication integrated into Implantable Medical Devices (IMDs), such as the cardiac pacemaker. This method employed two inductors, one within the IMD and the other external to the body, to transmit data over short distances when aligned closely. However, this technology faced limitations due to potential misalignment, slow data transfer rates, and restricted communication distances. To address these issues, Radio Frequency (RF) antennas were introduced. Commonly used frequency bands for these antennas include the Medical Device Radio Communication Service (MedRadio) band (401-406 MHz) [54] and the Industrial, Scientific, and Medical (ISM) band (2.4-2.5 GHz) [54]. The choice of frequency band depends significantly on the application, balancing factors like tissue conductivity and communication speed [54].

Medical electronic devices are categorized based on the protocols and standards they use. The Wireless Medical Telemetry Services (WMTS) cater to wearable devices, while the Medical Implant Communications Service (MICS) is designated for implantable devices. The MICS band, ranging from 402 MHz to 405 MHz, is allocated by the European Telecommunications Standards Institute (ETSI) for implantable devices due to its lower power loss inside the human body [55]. In contrast, the ISM bands (433.1-434.8 MHz, 868-868.6 MHz, 902.8-928 MHz, and 2400-2500 MHz) are suggested for biotelemetry of implantable medical devices in various countries, particularly for subcutaneous applications [56]. Studies have shown that the MICS band achieves the minimum total loss between transmitter and receiver antennas, making it suitable for deep implanted antennas such as those used in capsule endoscopy [57], [58], [59], [60], [61].

The communication channels for implantable devices are diverse. One scenario involves communication between an implantable antenna and an external device, known as in/off-body communication. The external device, typically a control unit, sends and receives data observed by a physician or another person. For instance, a 3-D compact broadband implantable antenna was proposed for use in the MedRadio band

(401-406 MHz) for communication, with the ISM band (2.4-2.48 GHz) employed for wakeup signals. This design demonstrated gains of -28.95 dBi and 25.5 dBi, respectively [62].

In this work, we will operate at the 2.45 GHz frequency, which aligns with the Bluetooth frequency. This choice facilitates a wide range of applications since most wireless connections today utilize Bluetooth, enhancing the potential for integration with various devices such as smartwatches. Additionally, a half-wavelength dipole antenna will be employed due to its simplicity and ease of simulation. This approach ensures efficient and practical antenna design for biomedical applications.

b) Medium Selection

The main challenges of implantable antenna design arise from the complex environment of the human body, which significantly differs from free space. Human bodies consist of various tissues with high relative permittivity and conductivity, distributed asymmetrically, causing significant attenuation and reflection at tissue boundaries. These properties lead to additional losses when the electromagnetic wave travels from the human body to an external receiver, distinguishing near-field from far-field implantable communications. Near-field communication, where the receiver is directly attached to or placed close to the human body, experiences much smaller losses due to shorter distances [1].

Microwave penetration into human tissue is crucial for medical diagnosis, highly dependent on the dielectric and dispersive properties of the tissue, and the efficiency of the microwave radiator near human tissue [52], [53], [63]. The human body is a complex structure comprising various materials, with tissue characteristics expressed through dielectric permittivity (ϵ) and conductivity (γ) at microwave frequencies [64], [65], [66]. The dielectric properties of human tissues, including permittivity and conductivity, are essential in understanding the interactions between tissues and electromagnetic fields, influencing the design and performance of implantable antennas.

Dielectric permittivity and electrical conductivity, fundamental to understanding EM interactions with biological tissues, can be defined as complex quantities. Permittivity (ϵ) describes induced polarization and dipole alignment in the presence of an electric field, with the real part ($\text{Re}[\epsilon]$) representing the lossless component and the imaginary part ($\text{Im}[\epsilon]$) indicating energy losses [67]. Electrical conductivity measures the capacity of a material to allow free electric charges to circulate. This property is frequency (ω). For homogeneous, isotropic, and linear media, absolute permittivity is given by:

$$\epsilon(\omega)\epsilon_0 = \epsilon_0(\text{Re}[\epsilon] - i \text{Im}[\epsilon]) = \epsilon_0 \left(\text{Re}[\epsilon] - \frac{i\gamma(\omega)}{\omega\epsilon_0} \right) = \epsilon_0 \text{Re}[\epsilon](1 - i \tan \delta), \quad (1)$$

where ϵ_0 is the vacuum permittivity and ($\tan \delta$) the loss tangent that indicates the degree to which a medium is lossy. These properties significantly affect the propagation of EM waves, with higher attenuation rates in biological tissues due to losses and reflections at tissue interfaces and the air-body interface [68].

Designing antennas for operation near the human body requires accurate simulation of human tissues' complex structure and characteristics. Often, a homogeneous phantom is used to simplify simulations and reduce time, although this does not fully capture the inhomogeneous and frequency-dependent nature of human tissues. Despite these challenges, implantable antennas and on-body matched antennas have been successfully designed for various medical applications, enhancing impedance matching and signal penetration in human tissues [37], [69], [70], [71], [72], [73], [74], [75].

In this work that the medium which was selected due to the easier way for simulation environment was a fat of 30 [mm] thickness which the receiver dipole was placed. The permittivity for desired frequency that was selected according to literature searching was $\epsilon_1 = 5.28(1 - 0.14i)$ [41], [76], [77].

III.) Results

a) Computational Modeling

We consider a system of two antennas: the first one radiates into free space and provides the primary excitation while the second one is embedded into human tissue. The first dipole is placed at distance b from the air-fat interface and the second dipole at distance h from it, as shown in Fig. 2. The transmitter radiates at Bluetooth frequency $f \cong 2.45$ GHz, where the complex dielectric constant of human fat equals to: $\epsilon_1 \cong 5.28(1 - 0.14i)$.

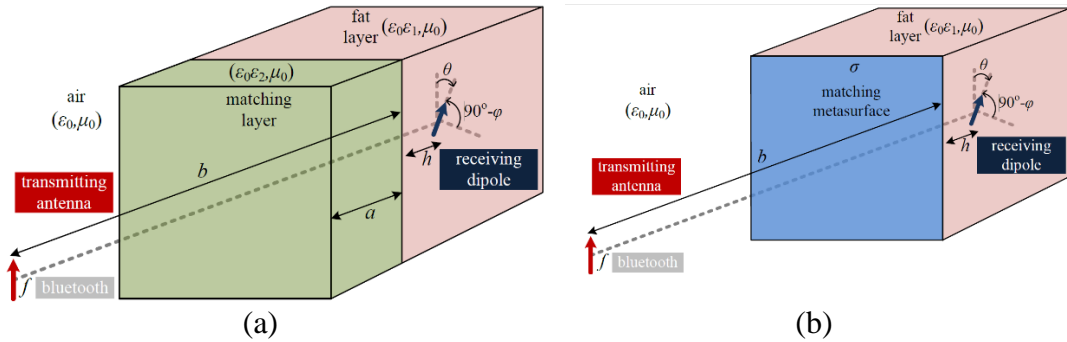


Figure 2.) The physical configuration of the examined setups. A transmitting dipole antenna operated at Bluetooth frequency $f \cong 2.45$ GHz illuminates human tissue located at distance b , into which another dipole tilted by angles (θ, φ) has been placed. To enhance the penetration of the electromagnetic signal into the fat host, we utilize: **(a)** a matching layer of thickness $a < b$ and relative permittivity ϵ_2 and **(b)** a matching metasurface of complex surface conductivity σ . The complex relative permittivity of the fat is denoted by ϵ_1

In order to maximize the coupling between the two antennas so that all the related diagnostic, monitoring and sensing bioelectromagnetic applications are better facilitated, we propose the deposition either of a dielectric layer of thickness $a < b$ and relative complex permittivity ϵ_2 (depicted in Fig. 2(a)) or a metasurface of complex surface conductivity σ (depicted in Fig. 2(b)). Since the orientation of the receiving

passive dipole may change into the tissue of the patient, we permit it to be misaligned with respect to the axis of the external source by angle θ and rotated by angle φ while being parallel to the boundary between the two media.

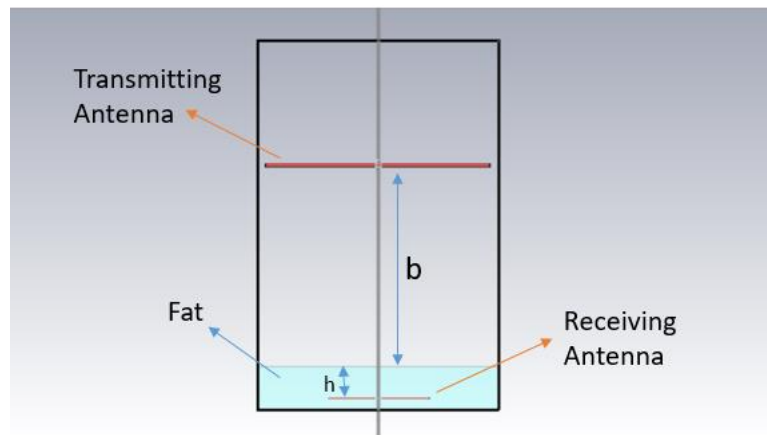


Figure 3.) Realistic set up of the two antennas system (transmitting, receiving) without any matching technique which was used for every simulation applied on COMSOL Multiphysics environment.

In this study, we utilized two simulation programs. Initially, the two-antenna system was modeled using the COMSOL Multiphysics computational program to evaluate the efficiency of each antenna as it is shown in Fig.3(a). The characteristics of the two half-wavelength dipole antennas were determined according to the following equations, First task was to determine the wavelength λ of the system on the desired frequency from , $\lambda = \frac{c}{f} \xrightarrow{\text{bluetooth}} \lambda = 122.5$ [mm]. Then based on λ the length of each dipole was computed with the length of transmitter from $L = \frac{\lambda}{2}$ and the same equation was used for the length of receiver but with the difference that the medium which will be placed was fat so the modification of the previous formula lead to $L_1 = \frac{\lambda}{2\sqrt{\epsilon_1}}$. Then an important calculation was to find the limits of each radiation region as it is demonstrated in Fig. 1 , so $Near_field < \lambda = 122.5$ [mm] while the transition region exists in the spectrum of 2 following wavelengths , 122.5 [mm] $< Transition < 245$ [mm] and finally the far field take place where the transition region ends and has no limit $Far_field > 2\lambda = 245$ [mm].

An optimization occurred for the radius of poles and the gap between them in order to tune each dipole on f_1 by computing the $|S_{11}|$ parameter which resembles the reflection coefficient of an antenna. The final values of characteristics are shown at Table 1 :

Table 1.) Final geometry characteristics of transmitting and receiving antenna after optimization, both tuned on $f \cong 2.45$ GHz		
Dipole	Transmitter	Receiver
Length	$L = 56$ [mm]	$L_1 = 26.63$ [mm]
Radius	$R = 0.37$ [mm]	$R_1 = 0.25$ [mm]

Gap	$G = 0.17[\text{mm}]$	$G_1 = 0.1[\text{mm}]$
-----	-----------------------	------------------------

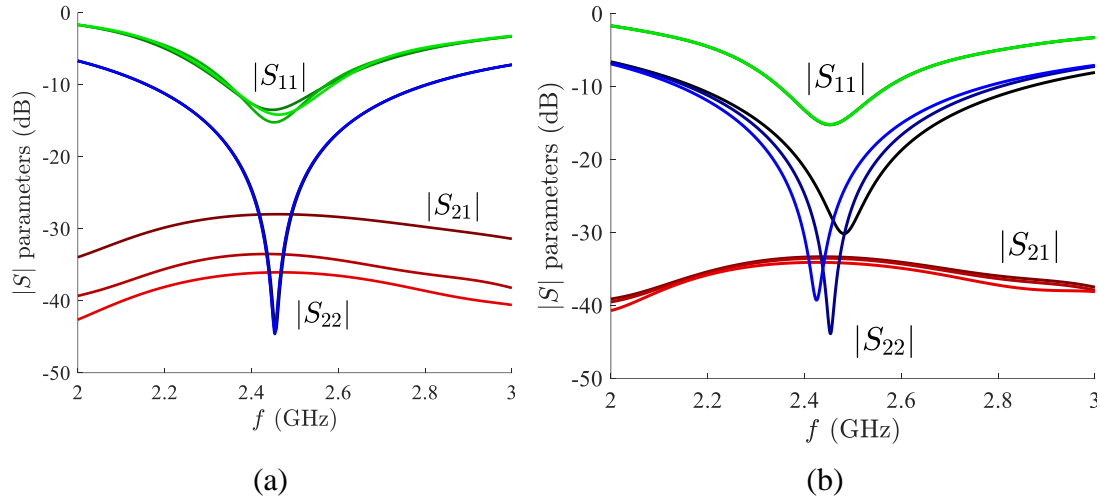


Figure 4.) The scattering parameters magnitudes of the system of the two dipole antennas in the absence of any matching equipment for: **(a)** $b = 100, 200, 300$ mm with $h = 15$ mm and **(b)** $h = 10, 15, 20$ mm with $b = 200$ mm. The lighter the color tone of the curve is, the larger the implicit parameter is selected.

In Fig. 4, we regard the initial system without any additional matching equipment and test the behavior of the two antennas in the spectral vicinity of Bluetooth frequency. In particular, we treat them as a two-port network and compute the scattering parameters as functions of the operational frequency f . In Fig. 4(a), we represent the magnitudes of S parameters in dB with respect to $2 \text{ GHz} < f < 3 \text{ GHz}$ for various distances b of the first antenna from the interface which covers all radiation fields as they computed from aforementioned equations ($b = 100, 200, 300$ mm); the lighter the used color is, the more distant the dipole is placed. One directly observes that, due to the different size of the two antennas, the reflections are stronger in the first one compared to those at the second one; indeed, the transmitting cylindrical dipole is lengthier and thicker compared to the receiving one [78]. What is noteworthy is that both $|S_{11}|$ and $|S_{22}|$ are minimized very close to Bluetooth frequency $f \cong 2.45$ GHz and in a manner not significantly dependent on the location b . Such a result is not coincidental since the characteristics of the antennas determining their resonances, have been previously optimized. As far as the transmission $|S_{21}|$ from one port to the other is concerned, it is obviously inversely proportional to the distance b since the directivities of the antennas are finite. Indeed, for increasing b , the radiated power is distributed across a larger surface and thus a smaller portion from it reaches the receiving antenna.

In Fig. 4(b), we show again the frequency dispersion of same quantities as in Fig. 4(a) but for several distances h of the second antenna into human tissue from the boundary ($h = 10, 15, 20$ mm). Similarly to Fig. 4(a), the reflections to the first antenna are not affected substantially by the placement of the port but still are minimized at the Bluetooth frequency $f \cong 2.45$ GHz, regardless of the selection of h . Moreover, $|S_{21}|$ is also practically independent from the distance h contrary to what is happening in Fig. 4(a); this is due to the small values of h since the receiver should stay into fat, below

the human skin. Interestingly, the reflection at the second antenna changes for different values of h since the formed Fabry-Perot cavities are resonating at different frequencies; however, all the three minima of the curves are close to our working frequency $f \cong 2.45$ GHz.

b) Mathematical Modeling

In order to understand better the conditions that lead to maximal coupling between the two dipoles, we introduce two one-dimensional analytically solvable models, one for each of the configurations of Fig. 2. The actual structures of Fig. 2 can be also treated in a rigorous manner but it involves integral equations [79], [80] where the field quantities are approximated by finite sums of basic functions and the final formulas are not physically interpretable.

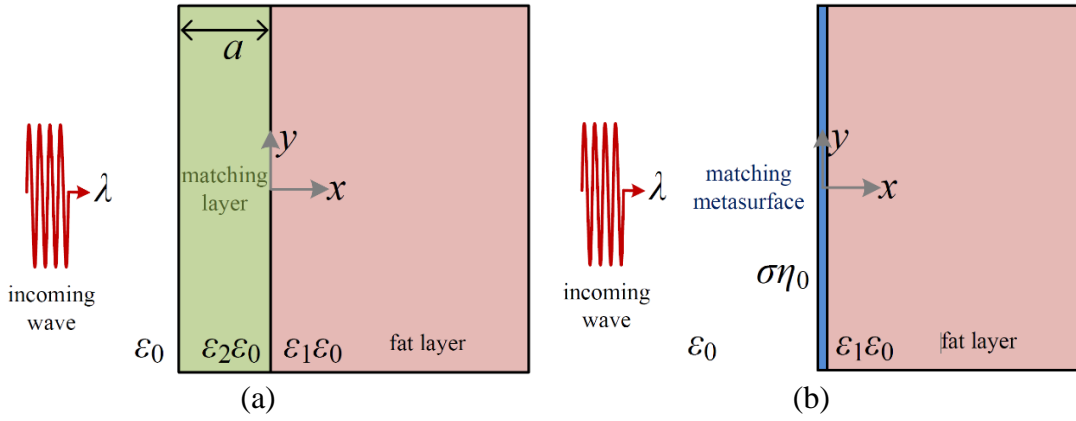


Figure 5.) Simplistic one-dimensional models for the two scenarios of Fig. 2. The receiving dipoles have been conditionally removed while the transmitted antennas have been replaced by normally incident waves of wavelength λ .

In Fig. 5(a), we consider as excitation into free space a normally incident plane wave of the same Bluetooth operational wavelength $\lambda \cong 122.5$ mm. If one ignores the receiving dipole, the reflection coefficient reads:

$$R_L = e^{2ik_0a} \frac{e^{ik_2a}(k_0-k_2)(k_1+k_2) - e^{-ik_2a}(k_1-k_2)(k_0+k_2)}{e^{ik_2a}(k_0-k_2)(k_1+k_2) - e^{-ik_2a}(k_1-k_2)(k_0-k_2)}, \quad (2)$$

where $k_0 = \frac{2\pi}{\lambda}$ is the wavenumber into air and $k_1 = k_0\sqrt{\epsilon_1}$, $k_2 = k_0\sqrt{\epsilon_2}$, the wavenumbers into fat and matching layer respectively.

By calling for perfect matching so that maximal power enters the area of the receiver (given the fact that the losses of the mediator layer are negligible), we derive the condition from (2):

$$R_L = 0 \rightarrow e^{4\pi i\sqrt{\epsilon_2}a/\lambda} = \frac{(1+\sqrt{\epsilon_2})(\sqrt{\epsilon_1}-\sqrt{\epsilon_2})}{(1-\sqrt{\epsilon_2})(\sqrt{\epsilon_1}+\sqrt{\epsilon_2})}. \quad (3)$$

If we assume that, apart from intermediate layer, the fat half-space is also lossless and non-plasmonic, the right-hand side of (3) is a real number. That forces the left-hand

side of (3) to take specific values (± 1); however, the equation $e^{4\pi i\sqrt{\varepsilon_2}a/\lambda} = 1$ leads to $\varepsilon_2 = 0$, which is rejected. Therefore, the perfect matching conditions take the form:

$$R_L \cong 0 \rightarrow \left\{ \frac{\alpha}{\lambda} \cong \frac{2m+1}{4\sqrt{\varepsilon_2}}, m \in N \text{ and } \varepsilon_2 \cong \sqrt{\varepsilon_1} \right\}. \quad (4)$$

The equalities are approximate since ε_1 in practice is a complex number.

In Fig. 5(b), we sketch the respective one-dimensional model once the matching metasurface is used. The boundary conditions between air with electromagnetic fields (\mathbf{E}, \mathbf{H}) and fat with electromagnetic fields ($\mathbf{E}_1, \mathbf{H}_1$) are given by [81]:

$$\begin{aligned} \hat{\mathbf{n}} \times (\mathbf{E}_1 - \mathbf{E})|_{x=0} &= 0, \\ \hat{\mathbf{n}} \times (\mathbf{H}_1 - \mathbf{H})|_{x=0} &= -\hat{\mathbf{n}} \times (\hat{\mathbf{n}} \times \mathbf{E})|_{x=0}, \end{aligned}$$

where $\hat{\mathbf{n}} = \hat{\mathbf{x}}$ is the unitary vector normal to the air/fat interface ($x = 0$), as defined in Fig. 3(b). By imposing them, we analytically derive the reflection coefficient:

$$R_M = \frac{1 - \sqrt{\varepsilon_1} - \sigma\eta_0}{1 + \sqrt{\varepsilon_1} + \sigma\eta_0}. \quad (5)$$

Apparently, the perfect matching condition reads from (5):

$$R_M = 0 \rightarrow \sigma = \frac{1 - \sqrt{\varepsilon_1}}{\eta_0}. \quad (6)$$

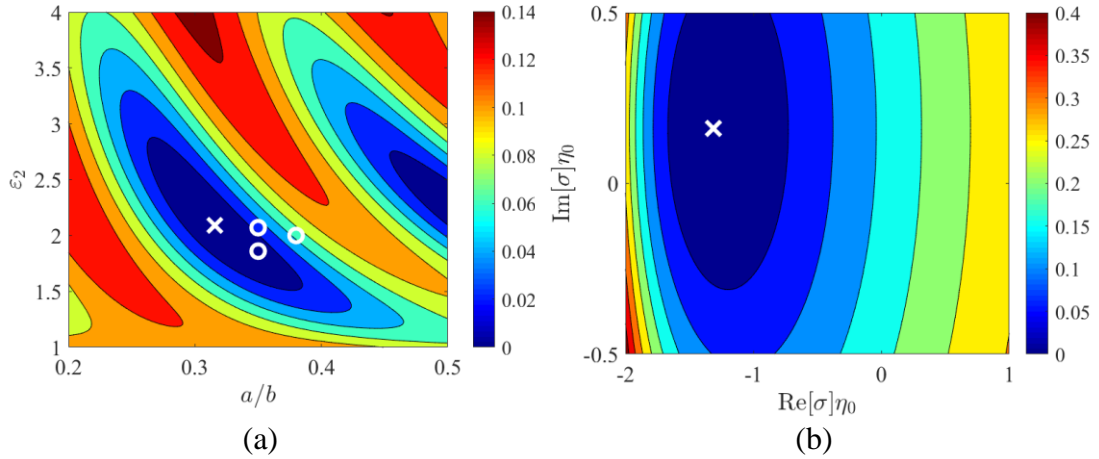


Figure 6.) (a) The magnitude of reflection coefficient $|R_L|$ from (1) as a function of relative thickness of the layer a/b and relative complex permittivity $\varepsilon_2(1 - i0.05)$. The circular markers denote optimal operation points of the actual system of Fig. 2(a) for various locations h of receiving dipole. (b) The magnitude of reflection coefficient $|R_M|$ from (4) as a function of real and the imaginary part of the relative complex surface conductivity $\sigma\eta_0$. Plot parameters: $\varepsilon_1 \cong 5.28(1 - 0.14i)$, $b = 200$ mm. The marker \times corresponds to the parametric point of minimum reflections.

In Fig. 6(a), we represent the magnitude of the reflection coefficient $|R_L|$ of analytical model of Fig. 5(a) with respect to normalized thickness of the layer a/b and the relative

permittivity of its medium ε_2 , in a contour plot. We use a fixed $b = 200$ mm even though is not a parameter of our model, in order to relate with our realistic setup of Fig. 2(a). One observes that $|R_L|$ is a periodic function of a , which is natural since condition (4) gives an infinite number of solutions ($m \in \mathbb{N}$ from (3)). The regime of minimum reflection is indicated by an \times marker which is in accordance with (4) and imposes maximal transmission into human tissue. On that variation map of $|R_L|$, we show three additional circular markers corresponding to the optimal parametric regimes of the actual configuration of Fig. 2(a), as obtained via numerical simulations. Each of them concerns a different placement h of the passive antenna, but all of them are close to the theoretical predicted one (marker \times). It is noted that, when increasing h , the realistic results tends to reach the analytical solution of (4).

In Fig. 6(b), we depict the magnitude reflection coefficient $|R_M|$ from (5) across the complex plane of surface conductivity $\sigma\eta_0$ multiply by the wave impedance of the space. Again the matching regime is denoted by the \times marker which gives the $\sigma\eta_0$ indicated by (6). By inspection of Fig. 6(b) one directly remarks that the equipotential contour lines around the optimal regime, resemble the shape of concentric circles. Indeed, the demand for constant and small magnitude $|R_M| \rightarrow 0$ from (5) gives the equation of the circle:

$$(\text{Re}[\sigma]\eta_0 - 1 + \text{Re}[\sqrt{\varepsilon_1}])^2 + (\text{Im}[\sigma]\eta_0 + \text{Im}[\sqrt{\varepsilon_1}])^2 = |R_M|^2.$$

It is noteworthy that, given the fact that $\text{Re}[\sqrt{\varepsilon_1}] > 1$, the surface conductivity that “unlocks” the structure to achieve perfect matching has a negative real part ($\text{Re}[\sigma] < 0$) which characterizes active structures. Therefore, the proposed remedy for poor coupling of Figs 2(b), 5(b) (matching layer) involves gain media; such a feature renders it fundamentally different from the solution described by Figs 2(a), 5(a) (matching metasurface) which incorporates only lossless substances. It can be also mentioned that the magnitude of the reflection coefficient $|R_M|$ may surpass unity as the amount of energy that the structure provide can be unbounded; it usually happens in parity-time symmetric configurations [82].

c) Optimal Matching Layer

Having understood the ranges within which the parameters (a, ε_2) of the matching layer should belong, based on the simplistic model of Fig. 5(a), in this Section, we again consider the actual structure of Fig. 2(a) comprising the two dipole antennas to numerically simulate it. The key metric in understanding how much the coupling between the two radiators has been improved is the ratio of the transmitted power P'_{tran} in the presence of the matching setup over the respective power P_{tran} in the absence of them. This quantity is denoted by Q and can be also given as the ratio of the square magnitudes of the respective S_{21} quantities characterizing the two two-port networks. The definition is given below and takes into account the misalignment angles (θ, φ) only for the improved structure (numerator, primed) so that it is always compared with the best possible case ($\theta = \varphi = 0$) of the initial structure (denominator, unprimed).

$$Q \equiv \frac{P'_{tran}(\theta, \varphi)}{P_{tran}(\theta=0, \varphi=0)} \cong \frac{|S'_{21}(\theta, \varphi)|^2}{|S_{21}(\theta=0, \varphi=0)|^2}. \quad (7)$$

It is important to stress that the value of Q is dependent on the sequence of twisting the receiving dipole with respect to angles (θ, φ) ; indeed, the obtained configurations are different for a different order of rotations. However, if one covers the entire range of angles $0 < \theta, \varphi < 90^\circ$, all possible misalignment cases are considered. In our examples, we will focus on scenarios that the twist with respect to φ (if there is any) happens first, followed by the one with respect to θ (if there is any).

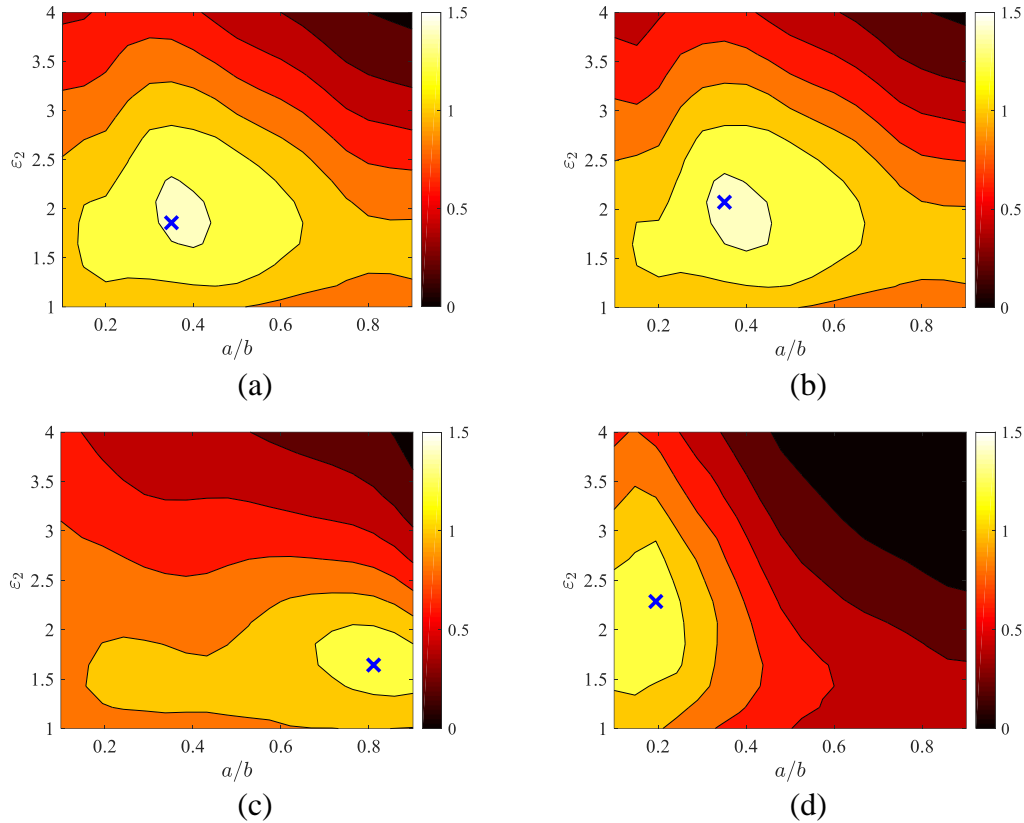


Figure 7.) The magnitude of the metric Q from (6) as a function of relative thickness of the layer a/b and relative complex permittivity $\varepsilon_2(1 - i0.05)$. **(a)** $b = 200$ mm and $h = 15$ mm, **(b)** $b = 200$ mm and $h = 10$ mm, **(c)** $b = 100$ mm and $h = 15$ mm, **(d)** $b = 300$ mm and $h = 15$ mm. Blue \times markers denote the optimal regimes.

In Fig. 7, we represent the metric Q defined by (7) on a map similar to that of Fig. 6(a) for several placements of the primary and secondary antenna. In Fig. 7(a), typical distances are assumed ($b = 200$ mm, $h = 15$ mm) and enhancement up to 50% of the transmitted power is recorded for relatively thin layers ($a/b \cong 0.35$). In Fig. 7(b), we change the location of the receiving dipole but the variation of Q does not perturb substantially since $h/\lambda \ll 1$; however, the optimal permittivity increases due to the shrunk of Fabry- Perot cavity between the air/layer boundary and the passive antenna. In Fig. 7(c), we locate the active dipole close to the boundary (smaller $b = 100$ mm) and, naturally, the optimal operation point appears at a higher ratio a/b while the slab permittivity ε_2 does not modify significantly compared to Figs. 7(a) since h remains

constant ($h = 15$ mm). In Fig. 7(d), we consider a more distant source ($b = 300$ mm) and obtain a similar response to that of Fig. 7(a) since the human tissue is positioned at the far field of the antenna; obviously, the highest Q emerges at a smaller a/b since b increased.

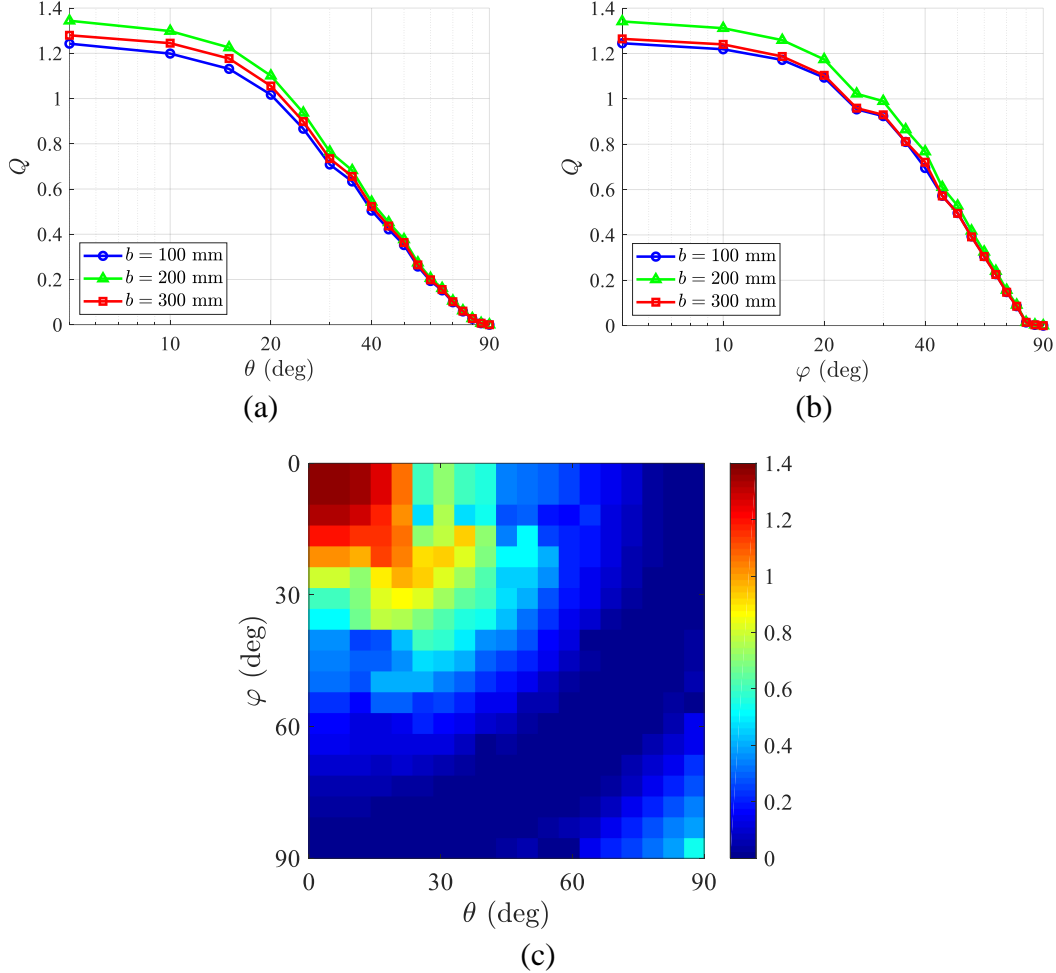


Figure 8.) The magnitude of the metric Q from (6), in the case of matching layer (Fig. 2(a)), as a function of: **(a)** dipole misalignment angle θ for $\varphi = 0$ and several distances b , **(b)** dipole rotation angle φ for $\theta = 0$ and several distances b , and **(c)** both misalignment angles (θ, φ) in contour plot for $b = 200$ mm. Plot parameters: $\epsilon_2 \cong 1.86$, $a \cong 0.35b$.

Unlike the transmitted antenna which is positioned with specific characteristics into the measurement setup, the orientation receiving one is not controlled since it is buried into human tissue. Therefore, it is meaningful to test the performance of our matching layer with respect to arbitrary misalignment angles (θ, φ) , as defined in Fig. 2(a). In Fig. 8(a), we consider the respective optimal configurations from Fig. 7 and represent the variations $Q = Q(\theta)$ for $\varphi = 0$ and various distances b ; it is, obviously, observed that they are decreasing functions of θ . It is also remarkable that even if the two dipole directions form angles as big as $\theta = 20^\circ$, we compute $Q > 1$ which means that our matching structure remains superior than a perfectly aligned but layer-free model. In Fig. 8(b), we represent the metric Q but time with respect to rotation angle φ , when

keeping $\theta = 0$. Once more the curves are downward sloping due to the polarization crosstalk while the transmissivity enhancement exhibits substantial robustness with respect to angle φ . It is noteworthy, that even if the design has been optimized for $b = 200$ mm giving $Q \cong 1.4$, it works well for alternative placements of the primary source; that is another finding that the proposed configurations remain beneficial for a parametrically perturbed environment.

Finally, in Fig. 8(c), we examine a receiving dipole that is simultaneously rotated by both the misalignment angles (θ, φ) with the one by φ first, for $b = 200$ mm as it is demonstrated in Fig. 9 ; to this end, we depict the distribution of $Q = Q(\theta, \varphi)$ in a contour plot. One can observe that the highest score occurs at $\theta = \varphi = 0$, which is obviously the starting point of both the respective curves for $b = 200$ mm in Figs 8(a),8(b) and also verifies that when the two antennas are in perfect parallel position the greatest transmission is achieved. In addition, when the sum of the two twists is constant, the response Q formulate zones of similar magnitude; indeed, for $\theta + \varphi \cong 120^\circ$ the results are worse than in the case that we maximally rotate the two antennas ($\theta = \varphi = 90^\circ$).

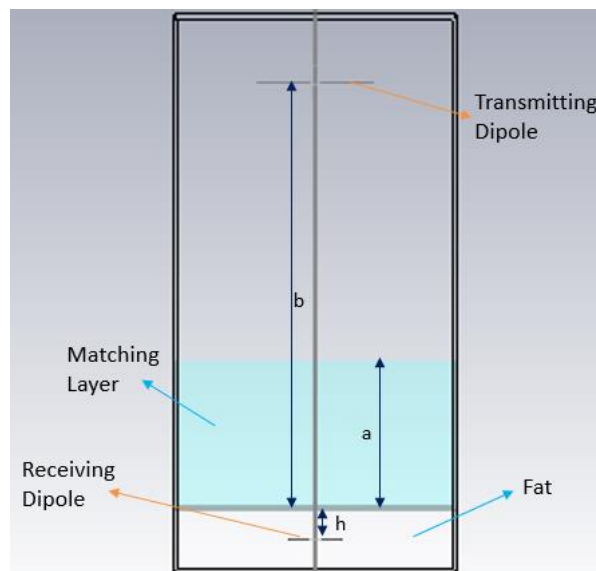


Figure 9.) Realistic configuration of the two antennas system (transmitting, receiving) applied matching layer technique for specific thickness a corresponding to $b = 200$ mm condition which was used for simulations processed on CST Studio Suite 2021.

d) Optimal Matching Metasurface

It would be interesting to observe the operation of deposited metasurfaces in trying to match the free-space with the receiver into the human tissue or, alternatively, to maximize Q , as defined from (7), in the actual system of dipoles. Given the fact that in our theoretical model of Fig. 4(b) the perfect matching occurred for $\text{Re}[\sigma] < 0$, according to (6) and Fig. 5(b), we will not rule out the usage of gain media in our simulations. Therefore, in Fig. 9(a), we represent Q (in dB) across the complex plane of surface conductivity $\sigma = \text{Re}[\sigma] + i \text{Im}[\sigma]$ and realize that a huge transmissivity enhancement of more than two orders of magnitude becomes feasible, which is attributed exactly to the active nature of the employed matching approach. It is noticeable that the emerged peak of Fig. 8(a) is accompanied by an anti-resonance, yielding minimum Q nearby, revealing an anticipated Fano resonance pattern.

One may wonder why the optimal operation point does not coincide with the corresponding one of the analytical model in Fig. 5(b), contrary to the apparent similarity between Figs 6(a) and 7(a) when the matching layer was used instead. The answer lies in the fact that the optimal layer is passive while optimal metasurfaces require gain materials. Indeed, the reflectivity and the transmissivity are not any more complementary each other; as a result, an active metasurface can support a giant transmission accompanied by a significant reflection. In this sense, our metasurface strategy does not concern matching the free space with the human fat but aims at optimally amplifying the incoming signal so that maximum penetration is achieved.

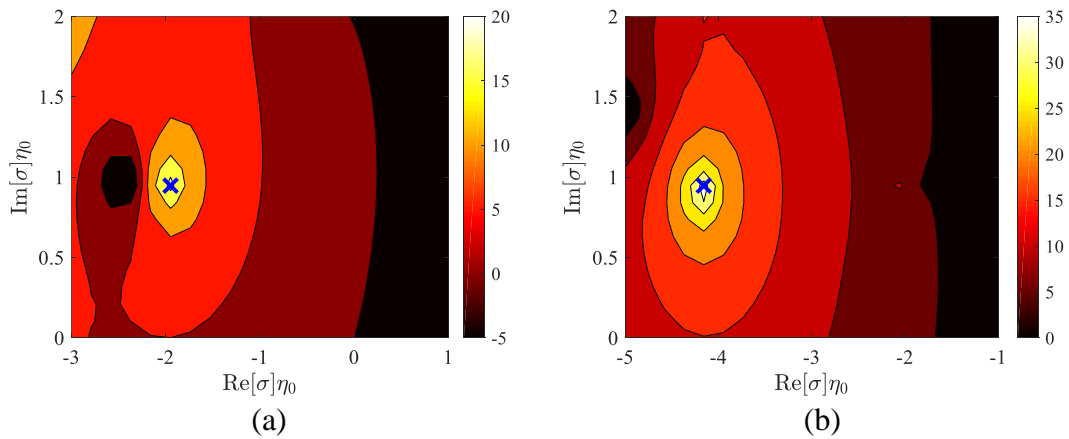


Figure 10.) The magnitude of the metric Q from (6) in dB across the complex plane of the dimensionless surface conductivity of the metasurface ($\text{Re}[\sigma]\eta_0$, $\text{Im}[\sigma]\eta_0$). (a) $b = 200$ mm and $h = 15$ mm, (b) $b = 100$ mm and $h = 15$ mm. Blue \times markers denote the optimal regimes.

In Fig. 10(b), we repeat the same calculations as in Fig. 10(a) but for a transmitting antenna located closer to human tissue ($b = 100$ mm). It is remarked that Q reaches

higher magnitudes compared to Fig. 10(a); that finding could be anticipated since the primary source is positioned near an active medium which, in turn, acts a secondary source that pumps new energy to the system. When it comes to the influence of gain $\text{Re}[\sigma]$ on our observable Q , it is not necessarily positive. Indeed, for higher $|\text{Re}[\sigma] < 0|$ than that corresponding to the maximum of Fig. 10(b), the performance of the respective metasurface is particularly poor, which validates the aforementioned point. As far as the imaginary part of σ is concerned, it just gives capacitive or inductive role to the metasurface and pushes it towards the reported resonances.

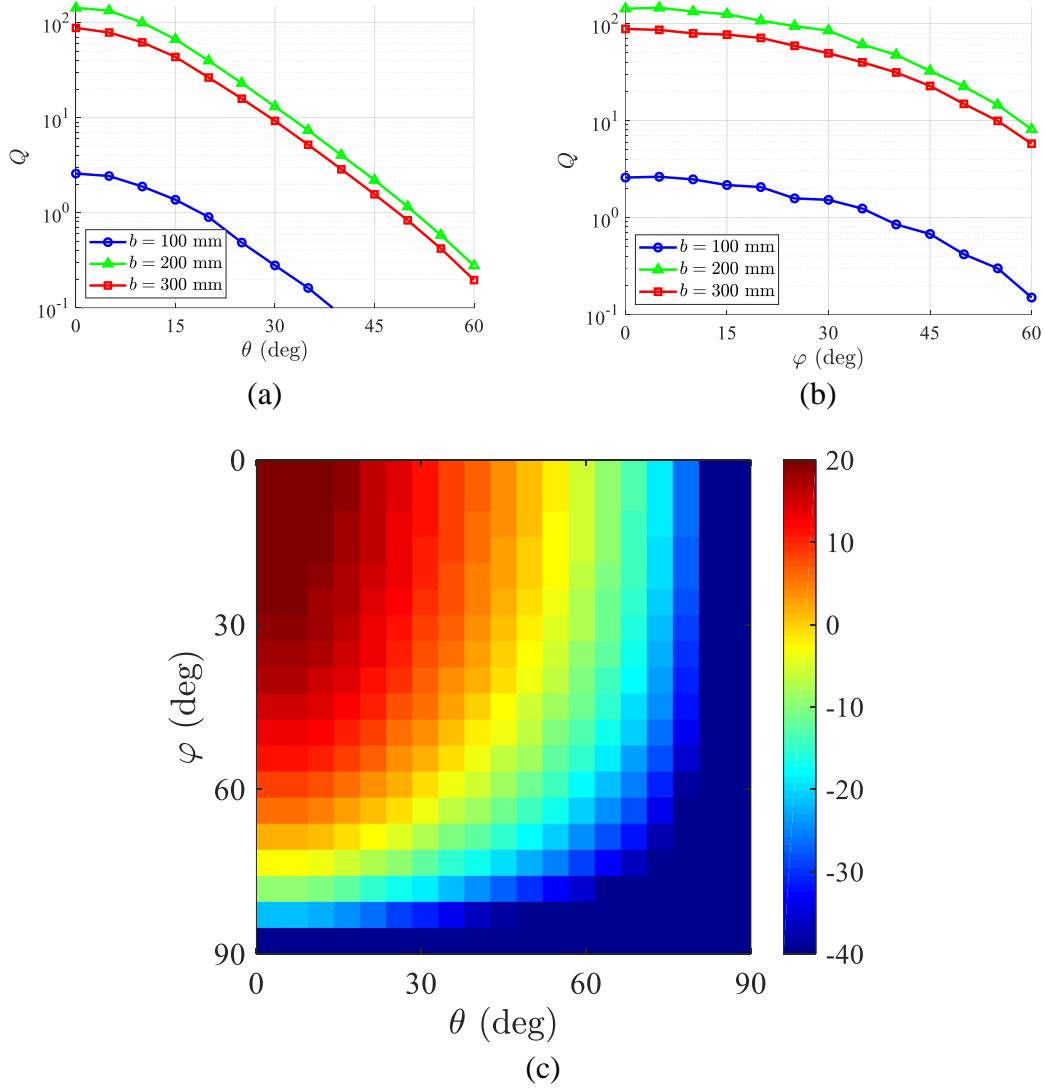


Figure 11.) The magnitude of the metric Q from (6), in the case of matching metasurface (Fig. 1(b)), as a function of: (a) dipole misalignment angle θ for $\varphi = 0$ and several distances b , (b) dipole rotation angle φ for $\theta = 0$ and several distances b , and (c) both misalignment angles (θ, φ) in contour plot for $b = 200$ mm. Plot parameters: $\sigma\eta_0 \cong -1.947 + 0.947i$.

In Fig. 11, we repeat the calculations from Fig. 7, utilizing the optimally designed active metasurfaces detailed in Fig. 10. The results highlight a notable improvement

in coupling efficiency and transmission performance due to the active nature of the metasurfaces. Specifically, in Fig. 11(a), we observe the Q metric of the optimal metasurface as a function of the misalignment angle θ with $\varphi = 0$, for various locations b of the external dipole. Substantial scores are recorded for both $b = 200$ mm and $b = 300$ mm for most directions within the cone $0 < \theta < 40^\circ$, attributed to the active properties of the metasurface. However, the performance drops significantly for $b = 100$ mm, despite the transmissivity enhancement observed in Fig. 10(b). This discrepancy suggests that the metasurface does not perform optimally at closer distances.

Further analysis in Fig. 11(b) demonstrates the Q score for the same structure as in Fig. 11(a) (optimized for $b = 200$ mm), as a function of the rotation angle φ with $\theta = 0$. The initial points of the three curves coincide with those in Fig. 11(a) since they all refer to aligned dipoles ($\theta = \varphi = 0$). However, the performance deteriorates more gradually when modifying the angle φ , as the receiving dipole remains parallel to the interface. Notably, a ten-fold enhancement is achieved for $\varphi = 60^\circ$ when the illuminating antenna is positioned at $b = 200$ mm, with similar high scores for $b = 300$ mm. Conversely, a dipole at $b = 100$ mm suffers from proximity to the interface, which significantly affects performance.

Moreover, an extensive analysis of the secondary antenna's mismatch across both angles (θ, φ) for a separation distance of $b = 200$ mm is presented in Fig. 11(c). This figure not only depicts the transmission distribution with the optimally designed metasurface but also presents the relationship $Q = Q(\theta, \varphi)$ through a contour plot. Compared to Fig. 8(c), it becomes evident that using a metasurface as a matching technique results in superior performance at $\theta = \varphi = 0$. This observation is consistent with the initial conditions depicted in Figs. 11(a) and 11(b), where the starting points also exhibit optimal performance. Interestingly, while achieving higher transmission in this configuration, there is a significantly more pronounced decrease in performance as the misalignment increases, compared to the matching layer technique. This trend is corroborated by the decreasing rates observed in Figs. 11(a) and 11(b). Nonetheless, the elevated transmission is not limited to a singular point but spans a range of angle combinations, specifically for $\theta < 15^\circ$ and $\varphi < 30^\circ$. Moreover, it is important to highlight that desired Q values greater than 1 are attained within a specific region where $\varphi \cong 70^\circ$ and $\theta \cong 50^\circ$. This indicates that while optimal alignment yields the highest transmission efficiency, the system maintains satisfactory performance over a broader range of angles, thereby offering greater flexibility and robustness in practical applications.

IV.) Conclusions and Future Considerations

External electromagnetic sources can be matched with implanted antennas into human tissue by tuning the operational frequency so that minimal reflections are achieved. While keeping the oscillating wavelength unaltered, we investigate the possibility of improving further the coupling between the two dipoles by depositing dielectric layers or metasurfaces across the air/skin interface. An equivalent one-dimensional semi-analytical model indicates that, at Bluetooth band, the optimal layer is an ordinary quarter-wavelength transformer but the optimal metasurface is an active one. Therefore, the two matching strategies are fundamentally different each other but each one possesses certain unique advantages:

the former one nullifies the reflections back to the source while the latter one can hugely boost transmissivity into the human skin. Extensive numeral simulations of the actual, three-dimensional systems validate the expected outcomes while the coupling performance of each layout has been tested successfully against misalignment of dipoles axes that cause polarization crosstalk. Our results may inspire further experimental efforts towards more efficient communication with implantable antennas that are supporting high data rates while being totally harmless for the patient.

An interesting expansion of the present work would be to focus on which media or meta-atoms can be used to build the proposed matching layers that are operable at the same frequencies and remedy potential availability limitations.

Moreover, one can use instead of wireless sources, wires connected with the equipment that is wrapped around the human skin and, in this way, materialize an analogue of active metasurface. Similar analytical and numerical techniques as the ones employed in this work may be implemented to understand the interference between the multiple sources that secures strong transmissivity into the human body. Due to reciprocity they will give a clearer picture about the structural and textural formations below the skin. In this way, a variety of minimally invasive biomedical processes can become easier to provide real-time information from the glucose content and the blood pressure to the distribution of virions or the size of protein cells.

A potential direction for future research involves constructing a realistic computational model of a more complex phantom that closely resembles specific parts of the human body, such as the arm or abdomen. This model should include multiple layers of biological tissues, such as skin and muscle. Although it may be challenging for simulation programs to accurately evaluate the same parameters in this more intricate setup, it would provide valuable insights for more specific applications derived from the suggestions made in this study.

Another critical aspect to assess is the Specific Absorption Rate (SAR) in this setup for each matching method. This evaluation is essential to determine whether the enhanced transmission leads to increased harm or reduced damage to human tissue from electromagnetic waves. Testing SAR values would ensure that any improvements in transmission efficiency do not compromise safety.

Additionally, conducting real-time experiments using this setup would be highly beneficial. Recording realistic results from such experiments would help ascertain the practical feasibility of the proposed configurations. Synthesizing the matching layer material with the specific material properties (complex permittivity) and thickness may pose a significant challenge, but it would yield valuable information for future biomedical applications. This endeavor, though difficult, is crucial for advancing the practical application of the research findings.

Bibliography

- [1] A. Kiourti and K. S. Nikita, 'A Review of Implantable Patch Antennas for Biomedical Telemetry: Challenges and Solutions [Wireless Corner]', *IEEE Antennas Propag. Mag.*, vol. 54, no. 3, pp. 210–228, Jun. 2012, doi: 10.1109/MAP.2012.6293992.
- [2] 'Design of the evolution of management strategies of heart failure patients with implantable defibrillators (EVOLVO) study to assess the ability of remote monitoring to treat and triage patients more effectively - PubMed'. Accessed: Jun. 10, 2024. [Online]. Available: <https://pubmed.ncbi.nlm.nih.gov/19538734/>
- [3] R. Sidhu, D. S. Sanders, A. J. Morris, and M. E. McAlindon, 'Guidelines on small bowel enteroscopy and capsule endoscopy in adults', *Gut*, vol. 57, no. 1, pp. 125–136, Jan. 2008, doi: 10.1136/gut.2007.129999.
- [4] A. K. Skrivervik, 'Implantable antennas: The challenge of efficiency', in *2013 7th European Conference on Antennas and Propagation (EuCAP)*, Apr. 2013, pp. 3627–3631. Accessed: Jun. 10, 2024. [Online]. Available: <https://ieeexplore.ieee.org/document/6546986>
- [5] A. Kiourti and K. S. Nikita, 'A Review of In-Body Biotelemetry Devices: Implantables, Ingestibles, and Injectables', *IEEE Trans. Biomed. Eng.*, vol. 64, no. 7, pp. 1422–1430, Jul. 2017, doi: 10.1109/TBME.2017.2668612.
- [6] A. Kiourti, K. A. Psathas, and K. S. Nikita, 'Implantable and ingestible medical devices with wireless telemetry functionalities: a review of current status and challenges', *Bioelectromagnetics*, vol. 35, no. 1, pp. 1–15, Jan. 2014, doi: 10.1002/bem.21813.
- [7] 'Design of a Dual-Band Implantable Antenna and Development of Skin Mimicking Gels for Continuous Glucose Monitoring | IEEE Journals & Magazine | IEEE Xplore'. Accessed: May 24, 2024. [Online]. Available: <https://ieeexplore.ieee.org/document/4470589>
- [8] M. L. Scarpello *et al.*, 'Design of an Implantable Slot Dipole Conformal Flexible Antenna for Biomedical Applications', *IEEE Trans. Antennas Propag.*, vol. 59, no. 10, pp. 3556–3564, Jul. 2011, doi: 10.1109/TAP.2011.2163761.
- [9] T. Karacolak, R. Cooper, and E. Topsakal, 'Electrical Properties of Rat Skin and Design of Implantable Antennas for Medical Wireless Telemetry', *IEEE Trans. Antennas Propag.*, vol. 57, no. 9, pp. 2806–2812, Sep. 2009, doi: 10.1109/TAP.2009.2027197.
- [10] A. Kiourti and K. S. Nikita, 'Miniature Scalp-Implantable Antennas for Telemetry in the MICS and ISM Bands: Design, Safety Considerations and Link Budget Analysis', *IEEE Trans. Antennas Propag.*, vol. 60, no. 8, pp. 3568–3575, Dec. 2012, doi: 10.1109/TAP.2012.2201078.
- [11] C. Liu, Y.-X. Guo, H. Sun, and S. Xiao, 'Design and Safety Considerations of an Implantable Rectenna for Far-Field Wireless Power Transfer', *IEEE Trans. Antennas Propag.*, vol. 62, no. 11, pp. 5798–5806, Aug. 2014, doi: 10.1109/TAP.2014.2352363.
- [12] A. Kiourti, J. R. Costa, C. A. Fernandes, and K. S. Nikita, 'A Broadband Implantable and a Dual-Band On-Body Repeater Antenna: Design and Transmission Performance', *IEEE Trans. Antennas Propag.*, vol. 62, no. 6, pp. 2899–2908, Jun. 2014, doi: 10.1109/TAP.2014.2310749.
- [13] C. Liu, Y.-X. Guo, and S. Xiao, 'Capacitively Loaded Circularly Polarized Implantable Patch Antenna for ISM Band Biomedical Applications', *IEEE Trans. Antennas Propag.*, vol. 62, no. 5, pp. 2407–2417, Feb. 2014, doi: 10.1109/TAP.2014.2307341.
- [14] X. Y. Liu, Z. T. Wu, Y. Fan, and E. M. Tentzeris, 'A Miniaturized CSRR Loaded Wide-Beamwidth Circularly Polarized Implantable Antenna for Subcutaneous Real-Time Glucose Monitoring', *IEEE Antennas Wirel. Propag. Lett.*, vol. 16, pp. 577–580, 2017, doi: 10.1109/LAWP.2016.2590477.

- [15] H. Basaeri, D. B. Christensen, and S. Roundy, 'A review of acoustic power transfer for bio-medical implants', *Smart Mater. Struct.*, vol. 25, no. 12, p. 123001, Aug. 2016, doi: 10.1088/0964-1726/25/12/123001.
- [16] N. Yu *et al.*, 'Light Propagation with Phase Discontinuities: Generalized Laws of Reflection and Refraction', *Science*, vol. 334, no. 6054, pp. 333–337, Oct. 2011, doi: 10.1126/science.1210713.
- [17] Z. Li *et al.*, 'Controlling propagation and coupling of waveguide modes using phase-gradient metasurfaces', *Nat. Nanotechnol.*, vol. 12, no. 7, pp. 675–683, Jul. 2017, doi: 10.1038/nnano.2017.50.
- [18] F. Qin *et al.*, 'Hybrid bilayer plasmonic metasurface efficiently manipulates visible light', *Sci. Adv.*, vol. 2, no. 1, p. e1501168, Jan. 2016, doi: 10.1126/sciadv.1501168.
- [19] C. Valagiannopoulos, T. A. Tsiftsis, and V. Kovanis, 'Metasurface-enabled interference mitigation in visible light communication architectures', *J. Opt.*, vol. 21, no. 11, p. 115702, Jul. 2019, doi: 10.1088/2040-8986/ab4c08.
- [20] C. H. Chu *et al.*, 'Active dielectric metasurface based on phase-change medium', *Laser Photonics Rev.*, vol. 10, no. 6, pp. 986–994, 2016, doi: 10.1002/lpor.201600106.
- [21] J. Lee *et al.*, 'Giant nonlinear response from plasmonic metasurfaces coupled to intersubband transitions', *Nature*, vol. 511, no. 7507, pp. 65–69, Jul. 2014, doi: 10.1038/nature13455.
- [22] M. A. Kats and F. Capasso, 'Optical absorbers based on strong interference in ultra-thin films', *Laser Photonics Rev.*, vol. 10, no. 5, pp. 735–749, 2016, doi: 10.1002/lpor.201600098.
- [23] T. A. Tsiftsis, C. Valagiannopoulos, H. Liu, A.-A. A. Boulogeorgos, and N. I. Miridakis, 'Metasurface-Coated Devices: A New Paradigm for Energy-Efficient and Secure 6G Communications', *IEEE Veh. Technol. Mag.*, vol. 17, no. 1, pp. 27–36, Mar. 2022, doi: 10.1109/MVT.2021.3119282.
- [24] Z. Li, X. Tian, C.-W. Qiu, and J. S. Ho, 'Metasurfaces for bioelectronics and healthcare', *Nat. Electron.*, vol. 4, no. 6, pp. 382–391, Jun. 2021, doi: 10.1038/s41928-021-00589-7.
- [25] C. Valagiannopoulos and A. Sihvola, 'Maximal interaction of electromagnetic radiation with corona virions', *Phys. Rev. B*, vol. 103, no. 1, p. 014114, Jan. 2021, doi: 10.1103/PhysRevB.103.014114.
- [26] K. Jaiswal, A. K. Patel, S. Yadav, S. Singh, R. S. Yadav, and R. Singh, 'Probe-Fed Wideband Implantable Microstrip Patch Antenna for Biomedical and Telemetry Applications', in *Soft Computing and Signal Processing*, vol. 900, J. Wang, G. R. M. Reddy, V. K. Prasad, and V. S. Reddy, Eds., in *Advances in Intelligent Systems and Computing*, vol. 900, Singapore: Springer Singapore, 2019, pp. 635–642. doi: 10.1007/978-981-13-3600-3_60.
- [27] 'Flexible antenna design on PDMS substrate for implantable bioelectronics applications - Fu - 2019 - ELECTROPHORESIS - Wiley Online Library'. Accessed: Jun. 11, 2024. [Online]. Available: <https://analyticalsciencejournals.onlinelibrary.wiley.com/doi/10.1002/elps.201800497>
- [28] S. H. Zainud-Deen, H. A. E.-A. Malhat, and A. A. Balabel, 'Octafilar Helical Antenna for Circular Polarization Wireless Capsule Endoscopy Applications', *Wirel. Pers. Commun.*, vol. 108, no. 1, pp. 569–579, Sep. 2019, doi: 10.1007/s11277-019-06418-7.
- [29] X. Wang, J. Shi, L. Xu, and J. Wang, 'A Wideband Miniaturized Implantable Antenna for Biomedical Application at HBC Band', in *2018 Cross Strait Quad-Regional Radio Science and Wireless Technology Conference (CSQRWC)*, Jul. 2018, pp. 1–3. doi: 10.1109/CSQRWC.2018.8455727.
- [30] S. H. Lee, K. Chang, K. J. Kim, and Y. J. Yoon, 'A conical spiral antenna for wideband capsule endoscope system', in *2008 IEEE Antennas and Propagation Society International Symposium*, Jul. 2008, pp. 1–4. doi: 10.1109/APS.2008.4619695.

- [31] R. Li, Y.-X. Guo, and G. Du, 'A Conformal Circularly Polarized Antenna for Wireless Capsule Endoscope Systems', *IEEE Trans. Antennas Propag.*, vol. 66, no. 4, pp. 2119–2124, Apr. 2018, doi: 10.1109/TAP.2018.2804674.
- [32] S. Das and D. Mitra, 'A Compact Wideband Flexible Implantable Slot Antenna Design With Enhanced Gain', *IEEE Trans. Antennas Propag.*, vol. 66, no. 8, pp. 4309–4314, Aug. 2018, doi: 10.1109/TAP.2018.2836463.
- [33] K. Zhang, C. Liu, X. Liu, H. Guo, and X. Yang, 'Miniaturized Circularly Polarized Implantable Antenna for ISM-Band Biomedical Devices', *Int. J. Antennas Propag.*, vol. 2017, no. 1, p. 9750257, 2017, doi: 10.1155/2017/9750257.
- [34] 'Micromachines | Free Full-Text | A Compact Broadband Antenna with Dual-Resonance for Implantable Devices'. Accessed: Jun. 11, 2024. [Online]. Available: <https://www.mdpi.com/2072-666X/10/1/59>
- [35] 'Compact dual-band antenna with slotted ground for implantable applications - Luo - 2019 - Microwave and Optical Technology Letters - Wiley Online Library'. Accessed: Oct. 24, 2023. [Online]. Available: https://onlinelibrary.wiley.com/doi/abs/10.1002/mop.31718?af=R&utm_source=feedburner&utm_medium=feed&utm_campaign=Feed%3A+motl+%28MOP+Recently+Published+Articles%29
- [36] 'Circularly Polarized Annular Ring Antenna With Wide Axial-Ratio Bandwidth for Biomedical Applications | IEEE Journals & Magazine | IEEE Xplore'. Accessed: Jun. 11, 2024. [Online]. Available: <https://ieeexplore.ieee.org/document/8708287>
- [37] I. A. Shah, M. Zada, and H. Yoo, 'Design and Analysis of a Compact-Sized Multiband Spiral-Shaped Implantable Antenna for Scalp Implantable and Leadless Pacemaker Systems', *IEEE Trans. Antennas Propag.*, vol. 67, no. 6, pp. 4230–4234, Jun. 2019, doi: 10.1109/TAP.2019.2908252.
- [38] G. Samanta and D. Mitra, 'Dual-Band Circular Polarized Flexible Implantable Antenna Using Reactive Impedance Substrate', *IEEE Trans. Antennas Propag.*, vol. 67, no. 6, pp. 4218–4223, Jun. 2019, doi: 10.1109/TAP.2019.2905978.
- [39] S. A. Kumar and T. Shanmuganatham, 'Coplanar waveguide-fed ISM band implantable crossed-type triangular slot antenna for biomedical applications', *Int. J. Microw. Wirel. Technol.*, vol. 6, no. 2, pp. 167–172, Apr. 2014, doi: 10.1017/S1759078713000883.
- [40] H.-Y. Lin, M. Takahashi, K. Saito, and K. Ito, 'Performance of Implantable Folded Dipole Antenna for In-Body Wireless Communication', *IEEE Trans. Antennas Propag.*, vol. 61, no. 3, pp. 1363–1370, Mar. 2013, doi: 10.1109/TAP.2012.2227099.
- [41] S. Maity, K. R. Barman, and S. Bhattacharjee, 'Silicon-based technology: Circularly polarized microstrip patch antenna at ISM band with miniature structure using fractal geometry for biomedical application', *Microw. Opt. Technol. Lett.*, vol. 60, no. 1, pp. 93–101, Jan. 2018, doi: 10.1002/mop.30925.
- [42] 'Radiofrequency and Microwave Radiation - Overview | Occupational Safety and Health Administration'. Accessed: Jun. 18, 2024. [Online]. Available: <https://www.osha.gov/radiofrequency-and-microwave-radiation>
- [43] A. T. Mobashsher and A. M. Abbosh, 'Compact 3-D Slot-Loaded Folded Dipole Antenna With Unidirectional Radiation and Low Impulse Distortion for Head Imaging Applications', *IEEE Trans. Antennas Propag.*, vol. 64, no. 7, pp. 3245–3250, Jul. 2016, doi: 10.1109/TAP.2016.2560909.
- [44] S. Ahdi Rezaeieh, A. Zamani, and A. M. Abbosh, '3-D Wideband Antenna for Head-Imaging System with Performance Verification in Brain Tumor Detection', *IEEE Antennas Wirel. Propag. Lett.*, vol. 14, pp. 910–914, 2015, doi: 10.1109/LAWP.2014.2386852.

- [45] B. J. Mohammed, A. M. Abbosh, S. Mustafa, and D. Ireland, 'Microwave System for Head Imaging', *IEEE Trans. Instrum. Meas.*, vol. 63, no. 1, pp. 117–123, Jan. 2014, doi: 10.1109/TIM.2013.2277562.
- [46] Md. Rokunuzzaman, Md. Samsuzzaman, and M. T. Islam, 'Unidirectional Wideband 3-D Antenna for Human Head-Imaging Application', *IEEE Antennas Wirel. Propag. Lett.*, vol. 16, pp. 169–172, 2017, doi: 10.1109/LAWP.2016.2565610.
- [47] A. T. Mobashsher, A. Mahmoud, and A. M. Abbosh, 'Portable Wideband Microwave Imaging System for Intracranial Hemorrhage Detection Using Improved Back-projection Algorithm with Model of Effective Head Permittivity', *Sci. Rep.*, vol. 6, no. 1, p. 20459, Feb. 2016, doi: 10.1038/srep20459.
- [48] A. T. Mobashsher, K. S. Bialkowski, A. M. Abbosh, and S. Crozier, 'Design and Experimental Evaluation of a Non-Invasive Microwave Head Imaging System for Intracranial Haemorrhage Detection', *PLoS One*, vol. 11, no. 4, p. e0152351, 2016, doi: 10.1371/journal.pone.0152351.
- [49] M. A. Jamlos, A. H. Ismail, M. F. Jamlos, and A. Narbudowicz, 'Hybrid graphene–copper UWB array sensor for brain tumor detection via scattering parameters in microwave detection system', *Appl. Phys. A*, vol. 123, no. 1, p. 112, Jan. 2017, doi: 10.1007/s00339-016-0691-6.
- [50] A. T. Mobashsher, K. S. Bialkowski, and A. M. Abbosh, 'Design of Compact Cross-Fed Three-Dimensional Slot-Loaded Antenna and Its Application in Wideband Head Imaging System', *IEEE Antennas Wirel. Propag. Lett.*, vol. 15, pp. 1856–1860, 2016, doi: 10.1109/LAWP.2016.2539970.
- [51] H. Bahrami, S. A. Mirbozorgi, L. A. Rusch, and B. Gosselin, 'Biological Channel Modeling and Implantable UWB Antenna Design for Neural Recording Systems', *IEEE Trans. Biomed. Eng.*, vol. 62, no. 1, pp. 88–98, Jan. 2015, doi: 10.1109/TBME.2014.2339836.
- [52] A. S. Y. Poon, S. O'Driscoll, and T. H. Meng, 'Optimal Frequency for Wireless Power Transmission Into Dispersive Tissue', *IEEE Trans. Antennas Propag.*, vol. 58, no. 5, pp. 1739–1750, Feb. 2010, doi: 10.1109/TAP.2010.2044310.
- [53] R. Chandra, H. Zhou, I. Balasingham, and R. M. Narayanan, 'On the Opportunities and Challenges in Microwave Medical Sensing and Imaging', *IEEE Trans. Biomed. Eng.*, vol. 62, no. 7, pp. 1667–1682, Jul. 2015, doi: 10.1109/TBME.2015.2432137.
- [54] 'Medical Device Radiocommunications Service (MedRadio) | Federal Communications Commission'. Accessed: Jun. 11, 2024. [Online]. Available: <https://www.fcc.gov/medical-device-radiocommunications-service-medradio>
- [55] H. S. Savci, A. Sula, Z. Wang, N. S. Dogan, and E. Arvas, 'MICS transceivers: regulatory standards and applications [medical implant communications service]', in *Proceedings. IEEE SoutheastCon, 2005.*, Apr. 2005, pp. 179–182. doi: 10.1109/SECON.2005.1423241.
- [56] A. Sani, A. Alomainy, and Y. Hao, 'The effect of various human body tissue models on radiowave propagation from a bladder implanted wireless source', in *2009 IEEE Antennas and Propagation Society International Symposium*, Jun. 2009, pp. 1–4. doi: 10.1109/APS.2009.5171659.
- [57] A. Kiourti and K. S. Nikita, 'Detuning issues and performance of a novel implantable antenna for telemetry applications', in *2012 6th European Conference on Antennas and Propagation (EUCAP)*, Mar. 2012, pp. 746–749. doi: 10.1109/EuCAP.2012.6206560.
- [58] J. Lee and S. Nam, 'Q Evaluation of Small Insulated Antennas in a Lossy Medium and Practical Radiation Efficiency Estimation', in *2007 Korea-Japan Microwave Conference*, Aug. 2007, pp. 65–68. doi: 10.1109/KJMW.2007.4402241.
- [59] N. Cho, T. Roh, J. Bae, and H.-J. Yoo, 'A Planar MICS Band Antenna Combined With a Body Channel Communication Electrode for Body Sensor Network', *IEEE Trans. Microw. Theory Tech.*, vol. 57, no. 10, pp. 2515–2522, Jul. 2009, doi: 10.1109/TMTT.2009.2029952.

- [60] C. Buratti, R. D'Errico, M. Maman, F. Martelli, R. Rosini, and R. Verdone, 'Design of a body area network for medical applications: the WiserBAN project', in *Proceedings of the 4th International Symposium on Applied Sciences in Biomedical and Communication Technologies*, in ISABEL '11. New York, NY, USA: Association for Computing Machinery, Jul. 2011, pp. 1–5. doi: 10.1145/2093698.2093862.
- [61] S. Manafi and H. Deng, 'Design of a Small Modified Minkowski Fractal Antenna for Passive Deep Brain Stimulation Implants', *Int. J. Antennas Propag.*, vol. 2014, no. 1, p. 749043, 2014, doi: 10.1155/2014/749043.
- [62] C. Schmidt, F. Casado, A. Arriola, I. Ortego, P. D. Bradley, and D. Valderas, 'Broadband UHF Implanted 3-D Conformal Antenna Design and Characterization for In-Off Body Wireless Links', *IEEE Trans. Antennas Propag.*, vol. 62, no. 3, pp. 1433–1444, Mar. 2014, doi: 10.1109/TAP.2013.2295816.
- [63] A. Drossos, V. Santomaa, and N. Kuster, 'The dependence of electromagnetic energy absorption upon human head tissue composition in the frequency range of 300–3000 MHz', *IEEE Trans. Microw. Theory Tech.*, vol. 48, no. 11, pp. 1988–1995, Aug. 2000, doi: 10.1109/22.884187.
- [64] C. Gabriel, S. Gabriel, and E. Corthout, 'The dielectric properties of biological tissues: I. Literature survey', *Phys. Med. Biol.*, vol. 41, no. 11, pp. 2231–2249, Nov. 1996, doi: 10.1088/0031-9155/41/11/001.
- [65] S. Gabriel, R. W. Lau, and C. Gabriel, 'The dielectric properties of biological tissues: II. Measurements in the frequency range 10 Hz to 20 GHz', *Phys. Med. Biol.*, vol. 41, no. 11, p. 2251, Aug. 1996, doi: 10.1088/0031-9155/41/11/002.
- [66] S. Gabriel, R. W. Lau, and C. Gabriel, 'The dielectric properties of biological tissues: III. Parametric models for the dielectric spectrum of tissues', *Phys. Med. Biol.*, vol. 41, no. 11, p. 2271, Aug. 1996, doi: 10.1088/0031-9155/41/11/003.
- [67] S. Semenov and D. Corfield, 'Microwave Tomography for Brain Imaging: Feasibility Assessment for Stroke Detection', *Int. J. Antennas Propag.*, vol. 2008, Jan. 2008, doi: 10.1155/2008/254830.
- [68] M. A. Shokry and A. M. M. A. Allam, 'UWB antenna for brain stroke and brain tumour detection', in *2016 21st International Conference on Microwave, Radar and Wireless Communications (MIKON)*, Feb. 2016, pp. 1–3. doi: 10.1109/MIKON.2016.7491967.
- [69] M. Persson *et al.*, 'Microwave-based stroke diagnosis making global prehospital thrombolytic treatment possible', *IEEE Trans. Biomed. Eng.*, vol. 61, no. 11, pp. 2806–2817, Nov. 2014, doi: 10.1109/TBME.2014.2330554.
- [70] X. Li, M. Jalilvand, Y. L. Sit, and T. Zwick, 'A Compact Double-Layer On-Body Matched Bowtie Antenna for Medical Diagnosis', *IEEE Trans. Antennas Propag.*, vol. 62, no. 4, pp. 1808–1816, Apr. 2014, doi: 10.1109/TAP.2013.2297158.
- [71] Mohd. S. R. Bashri, T. Arslan, W. Zhou, and N. Haridas, 'Wearable device for microwave head imaging', in *2016 46th European Microwave Conference (EuMC)*, Jul. 2016, pp. 671–674. doi: 10.1109/EuMC.2016.7824432.
- [72] S. Ahdi Rezaeieh, A. Zamani, K. S. Bialkowski, and A. M. Abbosh, 'Foam Embedded Wideband Antenna Array for Early Congestive Heart Failure Detection With Tests Using Artificial Phantom With Animal Organs', *IEEE Trans. Antennas Propag.*, vol. 63, no. 11, pp. 5138–5143, Aug. 2015, doi: 10.1109/TAP.2015.2475606.
- [73] Z.-J. Yang, S.-Q. Xiao, L. Zhu, B.-Z. Wang, and H.-L. Tu, 'A Circularly Polarized Implantable Antenna for 2.4-GHz ISM Band Biomedical Applications', *IEEE Antennas Wirel. Propag. Lett.*, vol. 16, pp. 2554–2557, 2017, doi: 10.1109/LAWP.2017.2732460.
- [74] S. Ma, L. Sydänheimo, L. Ukkonen, and T. Björninen, 'Split-Ring Resonator Antenna System With Cortical Implant and Head-Worn Parts for Effective Far-Field Implant Communications', *IEEE Antennas Wirel. Propag. Lett.*, vol. 17, no. 4, pp. 710–713, Apr. 2018, doi: 10.1109/LAWP.2018.2812920.

- [75] Y. Zhang, C. Liu, X. Liu, K. Zhang, and X. Yang, 'A Wideband Circularly Polarized Implantable Antenna for 915 MHz ISM-Band Biotelemetry Devices', *IEEE Antennas Wirel. Propag. Lett.*, vol. 17, no. 8, pp. 1473–1477, Dec. 2018, doi: 10.1109/LAWP.2018.2849847.
- [76] D. Gopi, K. Kumar Naik, and S. Rani, 'Design of ISM Band CPW-fed SRR Patch Conformal Antenna for Bio-medical Applications', *IEEE Access*, vol. PP, pp. 1–1, Mar. 2019, doi: 10.1109/ACCESS.2019.2905661.
- [77] A. Christ, A. Klingenbock, T. Samaras, C. Goiceanu, and N. Kuster, 'The dependence of electromagnetic far-field absorption on body tissue composition in the frequency range from 300 MHz to 6 GHz', *IEEE Trans. Microw. Theory Tech.*, vol. 54, no. 5, pp. 2188–2195, Feb. 2006, doi: 10.1109/TMTT.2006.872789.
- [78] G. Fikioris and C. Valagiannopoulos, 'Input admittances arising from explicit solutions to integral equations for infinite-length dipole antennas', *Prog. Electromagn. Res.-Pier - PROG ELECTROMAGN RES*, vol. 55, pp. 285–306, Jan. 2005, doi: 10.2528/PIER05031701.
- [79] C. Valagiannopoulos, 'Closed-form solution to the scattering of a skew strip field by metallic pin in a slab', *Prog. Electromagn. Res.-Pier - PROG ELECTROMAGN RES*, pp. 1–21, Jan. 2008, doi: 10.2528/PIER07092206.
- [80] C. A. Valagiannopoulos and N. L. Tsitsas, 'Integral equation analysis of a low-profile receiving planar microstrip antenna with a cloaking superstrate', *Radio Sci.*, vol. 47, no. 2, 2012, doi: 10.1029/2011RS004878.
- [81] C. Valagiannopoulos, A. Sarsen, and A. Alù, 'Angular Memory of Photonic Metasurfaces', *IEEE Trans. Antennas Propag.*, vol. 69, no. 11, pp. 7720–7728, Aug. 2021, doi: 10.1109/TAP.2021.3083806.
- [82] C. A. Valagiannopoulos, F. Monticone, and A. Alù, 'PT-symmetric planar devices for field transformation and imaging', *J. Opt.*, vol. 18, no. 4, p. 044028, Dec. 2016, doi: 10.1088/2040-8978/18/4/044028.